

Resolved H I observations of local analogs to $z \sim 1$ luminous compact blue galaxies: evidence for rotation-supported disks

Katie Rabidoux, D.J. Pisano¹

*Department of Physics and Astronomy, West Virginia University, 135 Willey St., P.O. Box 6315
Morgantown, WV 26506, USA*

C. A. Garland

*Natural Sciences Department, Jeffords Science Center, Castleton State College, Castleton, VT
05735, USA*

Rafael Guzmán

*Department of Astronomy, University of Florida, 211 Bryant Space Science Center, P.O. Box
112055, Gainesville, FL 32611, USA*

Francisco J. Castander

Institut de Ciències de l'Espai, (ICE, IEEC/CSIC), E-08193, Bellaterra (Barcelona), Spain

Spencer Wolfe

*Department of Physics and Astronomy, West Virginia University, 135 Willey St., P.O. Box 6315
Morgantown, WV 26506, USA*

ABSTRACT

While bright, blue, compact galaxies are common at $z \sim 1$, they are relatively rare in the local universe, and their evolutionary paths are uncertain. We have obtained resolved H I observations of nine $z \sim 0$ luminous compact blue galaxies (LCBGs) using the Giant Metrewave Radio Telescope and Very Large Array in order to measure their kinematic and dynamical properties and better constrain their evolutionary possibilities. We find that the LCBGs in our sample are rotating galaxies that tend to have nearby companions, relatively high central velocity dispersions, and can have disturbed velocity fields. We compare our measurements to those previously made with single dishes and find that single dish measurements tend to overestimate LCBGs' rotation velocities and H I masses. We also compare the ratio of LCBGs' rotation velocities to their velocity dispersions to those of other types of galaxies and find that LCBGs are strongly

¹Adjunct Assistant Astronomer at National Radio Astronomy Observatory, P.O. Box 2, Rt. 28/92, Green Bank, WV 24944, USA

rotationally supported at large radii, similar to other types of disk galaxies, though within their half-light radii their $\text{H I } V_{\text{rot}}\sigma^{-1}$ values are comparable to stellar $V_{\text{rot}}\sigma^{-1}$ values of dwarf elliptical galaxies. We find that LCBGs’ disks on average are stable with respect to instabilities, though conditions may be conducive to local instabilities at the largest radii, which could lead to the formation of star-forming gas clumps in the disk, resulting eventually in a small central bulge or bar.

Subject headings: galaxies: evolution — galaxies: ISM — galaxies: kinematics and dynamics

1. Introduction

1.1. LCBGs: Analogs to $z \sim 1$ star-forming galaxies

Luminous compact blue galaxies (LCBGs) are a morphologically heterogeneous class of star-forming galaxies that are defined by their blue colors, high blue luminosities, compact sizes, and high surface brightnesses (Werk et al. 2004). LCBGs at $z < 1$ are selected to have optical properties that are consistent with the small, bright, blue galaxies that appear in deep field observations (Koo et al. 1994; Phillips et al. 1997; Werk et al. 2004). Their strong optical emission lines and blue continua suggest that LCBGs harbor diverse stellar populations, with a current starburst involving approximately a tenth of the galaxy’s mass coexisting with older cohorts of stars of approximately solar metallicity (Hammer et al. 2001; Guzmán et al. 2003; Hoyos et al. 2007). While they are blue and compact, LCBGs are too massive ($M_* \sim 10^9 M_\odot$, Guzmán et al. 2003; Garland et al. 2004; Tollerud et al. 2010), luminous ($L_B \sim 10^9 L_\odot$, Garland et al. 2004), and have metallicities too high ($12 + \log(\text{O}/\text{H}) \sim 8.5$, Tollerud et al. 2010) to be classified as Blue Compact Dwarfs.

LCBGs are common at intermediate redshifts. Koo et al. (1994) found that 30% of compact sources at $z \sim 0.1 - 0.7$ show strong, narrow emission lines characteristic of star formation. Guzmán et al. (1997) found that LCBGs compose 20% of the general field population of galaxies and contribute 45% of the total star formation rate density at $0.4 < z < 1$. Tollerud et al. (2010) found that LCBGs comprise $\sim 10\%$ of the total galaxy population with $M_B < -17$ and $\sim 5\%$ of the galaxies with $M_B < -16$ at a median redshift of $z = 0.49$, which they note is lower than the Guzmán et al. (1997) value likely due to the rapid evolution of LCBGs after $z \sim 1$. In contrast to their abundance at intermediate redshifts, LCBGs are a factor of ten rarer in number density in the local universe (Guzmán 2001). This discrepancy suggests that LCBGs are a progenitor population for one or more of the galaxy types prevalent at $z \sim 0$. Garland et al. (2014) recently confirmed that local LCBGs have similar morphologies, gas fractions, and specific star formation rates to higher-redshift star-forming galaxies. Following the definitions compiled by Werk et al. (2004) to select for local analogs of intermediate-redshift LCBGs, these galaxies have $B - V < 0.6$, $\text{SBe}(B) < 21.0 \text{ mag arcsec}^{-2}$, and $M_B < -18.5$.

LCBGs’ properties overlap with many similar types of galaxies that have been described in the literature, including Compact Galaxies (Phillips et al. 1997; Guzmán et al. 1997), Luminous Compact Galaxies (Hammer et al. 2001), and Blue Compact Galaxies (Koo et al. 1994; Guzmán 1999; Barton & van Zee 2001; Pisano et al. 2001). Cardamone et al. (2009) found that LCBGs overlap in blue luminosity, morphology, stellar mass, and metallicity with the Green Pea galaxies detected by Galaxy Zoo at $z \sim 0.1 - 0.4$. Heckman et al. (2005) found that the lower-mass examples of compact Ultraviolet Luminous Galaxies (UVLGs), which they identify as low-redshift analogs of high-redshift Lyman Break Galaxies (LBGs), overlap in mass with the higher-mass examples of compact galaxies discussed in Phillips et al. (1997). Similarly, Guzmán et al. (2003) and Hoyos et al. (2004) point out that some LCBGs could be low-mass, lower-redshift counterparts to LBGs, and France et al. (2010) have detected fine-structure emission lines of Si II that have been previously observed in $z \sim 3$ LBGs in a $z \sim 0.04$ LCBG, which they interpret as an indication that star formation processes may be related in both types of galaxies. It is useful to study $z \sim 0$ LCBGs, then, to better understand the properties of the types of galaxies that exist at higher redshifts.

LCBGs have heterogeneous morphologies. Many LCBGs appear to be the products of mergers, especially at intermediate redshift where the spatial density of galaxies was larger and mergers were more common (Amram & Östlin 2001). In particular, irregular morphologies are more common in LCBGs than in other blue compact galaxies (Östlin et al. 2001). Many LCBGs also have companions (Garland et al. 2004; Pérez-Gallego et al. 2010; Garland et al. 2014). At $z \sim 0.2 - 1.3$, 60% of LCBGs appear to have similar properties to local H II galaxies, while 40% of LCBGs resemble local starburst disk galaxies, and 90% seem to be small galaxies with some extension, but lacking large, faint disks (Noeske et al. 2006). Garland et al. (2014) find that 40% of local LCBGs are “clumpy”, which they define to mean three or more optical clumps. Werk et al. (2004) point out that LCBGs are also not a distinct class of galaxies in parameter space. They exist at the extreme blue, bright, and compact ends of the optical properties that serve to identify them, but they are not outliers along the continuum of observed properties for field galaxies at the redshifts at which they appear (see Figure 1 in Garland et al. 2004).

As LCBGs at $z \sim 0$ are rare compared to their number density at $z \sim 1$, it is likely that they evolve quickly once their current episodes of star formation end, though it is not known what types of galaxies LCBGs will subsequently become. It has been suggested that LCBGs could be undergoing their final phase of star formation, and will continue to passively evolve and fade to become today’s spheroidal or dwarf elliptical galaxies (Guzmán et al. 1997; Bershadsky et al. 2005) or faint, low-mass spiral galaxies (Phillips et al. 1997). Other authors have suggested that LCBGs could be spiral galaxies undergoing a burst of star formation as they form their bulges (Barton & van Zee 2001; Hammer et al. 2001; Barton et al. 2006). It has also been asserted that LCBGs are galaxies that only appear similar in unresolved optical images at intermediate redshift and are actually a diverse enough population that their evolutionary paths and end products are widely varied (Tollerud et al. 2010). As LCBGs are visible at a large range of redshifts, they are excellent candidates for studying galaxy evolution (Hoyos et al. 2007).

1.2. Goals

In order to determine possible evolutionary paths for LCBGs, it is necessary to have knowledge of their H I properties. Measuring the H I mass gives an estimate of the fuel available for star formation and constrains the duration of the current starburst. The internal kinematics of the H I and evidence of past interactions give clues regarding the starburst triggering and quenching mechanisms (Pisano et al. 2001), and can support or rule out disk or spheroid models of LCBGs’ morphology. To investigate the nature of these galaxies, we have studied a selection of local analogs to intermediate-redshift LCBGs. Previously, Garland et al. (2004, 2005, 2007) surveyed the optical, H I, and CO properties of Sloan Digital Sky Survey (SDSS)- and Markarian- selected LCBGs. They took H I and CO spectra of a large sample of LCBGs using single pointings (Garland et al. 2004, 2005). For their study, they selected local LCBG analogs having the same optical properties as intermediate-redshift LCBGs as outlined by Werk et al. (2004). Garland et al. (2007) also initiated follow-up mapping observations of four Markarian galaxies and one SDSS galaxy with the Very Large Array (VLA). In this paper, we follow up the previous Garland et al. studies with Giant Metrewave Radio Telescope (GMRT) and VLA H I observations of galaxies selected from the Garland et al. (2004) sample, plus one additional local LCBG.

An overarching goal of this paper is to compare the H I properties we derive from resolved observations of nearby LCBGs to the properties derived from unresolved single pointings. Since LCBGs are most common at redshifts where resolved H I studies are not possible, it is important for us to understand what information is lost in unresolved observations of these galaxies. To accurately predict their evolution, we must first know what available observations can definitively tell us.

Previous H I studies of local LCBGs have not had the spatial resolution to distinguish the target sources from their nearby companions. Therefore, another goal of our study is to identify H I-rich companions and signatures of interacting galaxies that were not resolved in the single-dish H I observations from Garland et al. (2004). Since H I gas traces a galaxy’s gravitational potential at a much larger radius than light from stars, our resolved H I observations could indicate locations conducive to interaction-driven star formation where it may not be obvious from optical observations. We therefore take advantage of the GMRT and VLA’s angular resolution to measure the extent of H I emission and identify signatures of rotation in order to calculate dynamical masses (M_{dyn}) for these LCBGs from measurements of rotation velocities (as opposed to estimating M_{dyn} from linewidths that could potentially be biased by the inclusion of nearby companions, tidal features, or non-rotation components). Coupled with the H I mass (M_{HI}), these measurements give us an estimate of how much gas is available for the continuation of the starburst. This constrains the evolutionary scenarios for LCBGs, as the bulge formation scenario would imply that LCBGs have higher M_{dyn} than have been sampled from the central bright cores of LCBGs at intermediate redshifts (e.g. Pisano et al. 2001), and the spheroidal/dwarf elliptical progenitor scenario requires LCBGs to undergo passive evolution after their current starburst (Guzmán 1999), which would limit their possible rotation velocities.

An additional goal of this paper is to determine whether LCBGs are rotationally-supported disk galaxies or dispersion-dominated bulges to better understand their likely future morphologies once their star formation has been quenched. Since our resolved study can also distinguish velocity dispersions from rotation velocities, we can compare their rotation velocities to their velocity dispersions and look for evidence of disklike or bulgelike behavior both at their outermost regions and their centers. We can also use the ratio of ordered to random motions and the gas fractions that we have measured to look for evidence of disk instabilities that could trigger star formation in these galaxies. These measurements will better constrain the future evolution of local LCBGs, and have strong implications for the possible evolutionary products of their $z \sim 1$ counterparts.

In this paper, we describe our sample of LCBGs in Section 2, discuss results in Section 3, and give our conclusions in Section 4. We briefly address the properties of each LCBG in the Appendix. We assume $H_0 = 70 \text{ km s}^{-1}\text{Mpc}^{-1}$ throughout this paper.

2. Sample Selection, Observations, and Data Reduction

2.1. Sample selection

We chose nine galaxies from the SDSS- and Markarian-selected single-dish sample of LCBGs that Garland et al. (2004) observed with the Green Bank Telescope (GBT). We also included an additional SDSS galaxy (SDSS0125+0110) in our sample, selected from the single-dish sample of LCBGs that Garland et al. (in prep) observed with Arecibo. The Garland et al. samples were chosen for their blue colors, high luminosities, and compact appearances similar to properties outlined by Werk et al. (2004, see Garland et al. (2004) for a more detailed discussion of the selection criteria). We selected sources that had not been previously observed in H I emission at high resolution with interferometers. The galaxies we observed span the full range of colors of the GBT sample, but do not include the very brightest or most compact galaxies in the GBT sample that Garland et al. (2004) observed. We made sure to include galaxies with and without companions. We show the optical properties of the galaxies in our sample in Table 1 calculated using SDSS Data Release 7 magnitudes and radii (DR7, Abazajian et al. 2009) using the equations in Section 2.1.2 of Garland et al. (2004). The galaxies in our sample were strong detections in single-dish H I observations (Garland et al. 2004), which makes them good candidates for interferometer observations. The galaxies in our sample have heterogeneous morphologies, including isolated spiral galaxies, galaxies with tidal tails, multiple galaxies in a common H I envelope, galaxies with distant companions, and galaxies with disturbed gas components. One source (SDSS1319+5253) contains three galaxies in a common H I envelope, one of which (SBS 1317+523B) is an LCBG. The galaxy that was not included in the original Garland et al. (2004) sample (SDSS0125+0110) is not consistent with LCBG optical parameters when using the photometry of DR7. As its optical properties remain close to the LCBG optical cuts described by Werk et al. (2004), and remain within optical properties described by other authors (for example, Guzmán et al. 1997), we include it in

our analysis. We discuss each galaxy individually in the Appendix.

2.2. GMRT observations and reduction

Of our sample of nine galaxies, we observed eight with the GMRT near Pune, India. The GMRT is comprised of 30 antennas in a fixed Y-configuration with 14 antennas within 1 km and a maximum baseline of 25 km. We observed five galaxies (SDSS0728+3532, SDSS0934+0014, SDSS0936+0106, SDSS1319+5253, and SDSS1402+0955) in January of 2006, and three galaxies (SDSS0119+1452, SDSS0125+0110, and SDSS1507+5511) in January 2007. We observed each galaxy during a separate observing session with observations of flux calibrators 3C48, 3C147, and/or 3C286 at the beginning and end of the observing run. We interspersed observations of a bright, unresolved, nearby phase calibrator every ~ 40 minutes that we selected from the VLA Calibrator manual for a typical observing session of ~ 9 hours. We flagged and calibrated the data using the Astronomical Image Processing System (AIPS)² data reduction package using the standard procedures. For the GMRT this requires doing an initial calibration for a single, RFI-free channel before flagging and calibrating the full observing band. We made data cubes from the inner 50 channels (out of an original 128 channels with a channel width of ~ 13.7 km s⁻¹) using the AIPS task IMAGR. For each galaxy, we made two different cubes: a “low-resolution” cube (typically $\sim 50'' - 60''$) made from baselines shorter than 5 k λ , and a “high-resolution” cube (typically $5'' - 20''$) made with a larger UV range (made from baselines out to 50 k $\lambda - 120$ k λ). When making the high-resolution cubes, we chose robustness parameters, UV tapers, and UV ranges for each galaxy in order to maximize the resolution while maintaining a high level of signal to noise. We cleaned the data cubes using the number of iterations necessary for the total flux of the clean components in a central channel to reach a plateau so as not to incorporate too many negative clean components. See Table 2 for the imaging parameters used for each galaxy.

We used the high-resolution data cubes to make Moment 0 (total intensity), Moment 1 (intensity-weighted velocity), and Moment 2 (velocity dispersion) maps for each LCBG using the AIPS task MOMNT. These moment maps are shown in Figures 1 - 8. We also made low-resolution Moment 0 maps, shown in Figure 10. We typically clipped the high-resolution moment maps at the $2 - 3\sigma$ level, where we measured σ from the RMS in an emission-free channel. We chose this noise cut to maximize the galaxy emission shown in the moment maps, while minimizing the noise shown. We made an effort to include companions and preserve extended structures with lower column densities when possible in order to more fully show the morphology of these galaxies.

²aips.nrao.edu

2.3. VLA observation and reduction of Mrk 325

We observed the final galaxy, Mrk 325, with the VLA in the B and C configurations in December 2003 and November 2002 as part of projects AP463 and AP438, respectively. We also used data from the VLA archive taken as part of project AM361 in May 1992 and project AN62 in November 1993. In all cases, we performed flux calibration via observations of 3C48 or 3C286, and phase calibration through regular observations of J2254+247 (B2251+244). We carried out the data reduction for each configuration separately in the usual manner using AIPS. Because the pointing center for the D configuration observations was different than the B and C configuration data, we made the data cubes by mosaicking the observations in Miriad³. We made high-resolution and low-resolution moment maps for Mrk 325 in the same way as described in Section 2.2, shown in Figures 9 - 10.

3. Results

3.1. H I intensity maps, linewidths, and masses

The high-resolution Moment 0 maps in Figures 1-9 (the top right image in each figure) show heterogeneous H I morphologies, though the LCBGs have in common that the H I emission is centrally peaked, coincides with the center of the optical emission, and extends in an envelope to a radius larger than their stellar radii. Seven (78%) of the galaxies have companions that are detected in our H I maps (see Table 3). In addition, seven of the LCBGs have H I gas that appears disturbed.

We measured H I profiles for each LCBG using the AIPS task ISPEC using the low-resolution data cubes in order to correct for missing short spacings. We chose spatial boundaries for ISPEC using the extent of each LCBG’s H I emission in low-resolution Moment 0 maps. In the case of multiple galaxies in a common H I envelope, we measured the H I profile of the entire envelope because identifying boundaries for each galaxy while excluding H I emission associated with other galaxies or tidal features in the envelope introduced large uncertainties. We note that this means that measurements of quantities such as M_{HI} using the H I profiles of LCBGs in larger envelopes also encompass the entire envelope. We calculated an integrated flux for each galaxy by summing the flux in each channel within the first crossing at 0 mJy on each side of the peak and multiplying the sum by one channel width. We then calculated M_{HI} for each galaxy (or group of galaxies, in the case of systems with multiple galaxies sharing a common H I envelope) using the equation

$$\left(\frac{M_{\text{HI}}}{M_{\odot}}\right) = 2.356 \times 10^5 \left(\frac{D_{\text{HI}}}{\text{Mpc}}\right)^2 \frac{\int S \, dv}{\text{Jy km s}^{-1}} \quad (1)$$

³<http://carma.astro.umd.edu/miriad/>

where $\int S \, dv$ is the integrated flux within the spectrum’s crossing of 0 mJy and D_{HI} is the distance derived from dividing the recession velocity by the Hubble constant. The H I profile properties for each galaxy are listed in Table 4.

We compare the M_{HI} we measure for the LCBGs in our sample to those measured from the integrated line profiles observed by Garland et al. (2004) for the same LCBGs using single-dish observations in Table 4. Many of the LCBGs that Garland et al. (2004) detected had optical companions within the GBT beam. If the companions contain H I, they will add emission to the observed H I spectrum, and thus increase the measured M_{HI} . We flag the galaxies that Garland et al. (2004) identified as having companions within the GBT beam in Table 4.

In contrast to previous single-dish observations, our observations can spatially resolve the LCBGs from their companions. Thus, the M_{HI} that we measure from integrating over the intensities measured in each velocity channel within the spatial boundaries of each galaxy’s H I map are more likely to reflect the true M_{HI} of the target galaxies than those measured from integrating over the H I spectrum measured with an unresolved single pointing. In addition, having unresolved companions or tidal features in the beam can act to broaden a galaxy’s observed linewidth, and thus increase its inferred rotation velocity. Since LCBGs’ possible evolutionary scenarios depend on whether they are rotation-dominated, dispersion-dominated, or show signatures of interactions, it is important to determine whether LCBGs’ linewidths can be interpreted as the result of rotation. We discuss this further in Section 3.4.

3.2. Companions, mergers, and interactions

It has been hypothesized that LCBGs’ bright, blue, strongly star-forming appearances are due to star formation triggered by major and minor mergers (Amram & Östlin 2001; Östlin et al. 2001). These authors point out that LCBGs tend to have asymmetrical stellar distributions and non-uniform rotation curves, which are suggestive of mergers and interactions. In contrast, Werk et al. (2004) find that the majority of their sample of local LCBGs have symmetric morphologies. It is known that star formation can be triggered by mergers and interactions, so it would not be surprising if LCBGs were merger-driven. However, Garland et al. (2014) found using optical data that only 20% of the galaxies in their sample of local ($D < 76$ Mpc) LCBGs are in merging systems. In our sample, two of the nine galaxies have H I gas that overlaps with the gas of another galaxy, which is consistent with the merger rate of the Garland et al. (2014) sample. The LCBGs in our sample do not seem to require mergers to trigger their star formation, which is consistent with the relatively low percentage of LCBGs in merging systems.

Even though LCBGs are not preferentially mergers, they are commonly found in denser environments where close encounters with other galaxies that disturb their gas are more likely. Garland et al. (2014) found that in their sample, 40% of LCBGs are found in clusters. Crawford et al. (2011) found that from $0.5 < z < 1.0$, LCBGs are more likely to reside in denser environments at lower

redshifts than at higher redshifts, and Crawford et al. (2014) found that LCBGs tend to reside in the outer regions of clusters. Those authors hypothesize that in intermediate-redshift clusters, LCBGs are gas-rich blue galaxies whose star formation is triggered during their first infall into the cluster (Crawford et al. 2011, 2014). The LCBGs in our sample tend to have other galaxies nearby. In our sample, seven out of nine LCBGs have companions within one GBT beamwidth ($\sim 9'$ at 1.4 GHz), and three of the nine LCBGs have companions within one Arecibo beamwidth ($\sim 3'$ at 1.4 GHz). Six out of those seven LCBGs with companions have companions that we detect in our H I maps, and five of those seven have detected companions within ~ 10 times the LCBGs' H I radii (R_{HI}) and within 100 km s^{-1} of the LCBGs' systemic velocities. Seven of the nine LCBGs have disturbed gas properties that may be the result of an interaction with a companion, such as irregular morphologies, H I major axes that are offset in position angle from optical major axes, and disturbed velocity fields. Because this is not the case for every LCBG in our sample, we do not have strong evidence from this study that star formation in LCBGs *must* be triggered solely by interactions, though interactions may contribute to the star formation properties of some LCBGs. We discuss alternative scenarios for star formation in LCBGs in Section 3.6.1.

3.3. Velocity measurements

As is shown in the high-resolution Moment 1 maps (the bottom left images in Figures 1-8), all of the LCBGs in our sample show evidence of rotation. We measured systemic and rotation velocities (V_{rot}) for the LCBGs in our sample using the high-resolution Moment 1 maps for each LCBG both by measuring a slice of velocities along the galaxies' major axes and by fitting rotation curves to each galaxy's velocity field. We then calculated M_{dyn} for each LCBG using both of these V_{rot} using the equation

$$M_{\text{dyn}} = \frac{V_{\text{rot}}^2 \times R}{G} \quad (2)$$

where R is the radius at which V_{rot} is measured (and within which M_{dyn} applies). V_{rot} is corrected for inclination by

$$V_{\text{rot}} = \frac{V_{\text{measured}}}{\sin i} \quad (3)$$

where i is either the optical inclination taken from Hyperleda⁴ (for V_{rot} found using a slice across the major axis, as described in Section 3.3.1), or the inclination fitted to the velocity field by the AIPS task GAL (for V_{rot} computed from rotation curve fitting, as described in Section 3.3.2).

⁴<http://atlas.obs-hp.fr/hyperleda/>

3.3.1. Velocities from a slice along the major axis

The most reliable method of determining V_{rot} for each LCBG was to measure the velocities corresponding to the positions along the galaxies’ major axes. We determined the major axis of each galaxy using a visual inspection of their Moment 1 maps to identify features of rotation. This method produced measured, rather than fit, rotation curves from which we measured V_{rot} at the half-light radius (R_{eff}), the extent of ongoing star formation ($R_{25}(\text{B})$), the radius at which the galaxy has $\text{SBe}(\text{B}) = 25 \text{ mag arcsec}^{-2}$) and the extent of neutral hydrogen (R_{HI} , calculated as half of the galaxy’s diameter across its major axis between locations with a column density of $1 \text{ M}_{\odot} \text{ pc}^{-2}$). We note that while this method produced reliable values of V_{rot} , these velocities are only valid along the H I major axis. Values of V_{rot} corrected for inclination are uncertain due to using the galaxies’ optical inclinations, which may not match the inclination of the galaxies’ H I disks. We also calculated recession velocities as the velocity halfway between the velocities at each R_{HI} edge along the major axis, and M_{dyn} using V_{rot} at $R_{25}(\text{B})$ and R_{HI} . We report these values in Table 5 and display the rotation curves and major axis locations in Figure 11.

3.3.2. Rotation curve fitting

Because their Moment 1 maps all show a velocity gradient, with an identifiable major axis, it appears from the maps of the galaxies’ velocity fields that all of the galaxies, with the possible exceptions of SDSS0934+0014 and Mrk 325, are dominated by ordered rotation. This is the case even for the galaxies with companions, interactions, tidal tails, and otherwise disturbed gas. We fit rotation curves using the AIPS task GAL to each of these LCBGs to determine their H I centers, V_{rot} , recession velocities, and inclinations. We used the high-resolution Moment 1 maps as the maps to be fit, and used the corresponding Moment 0 maps at the same resolution as weights to better identify the locations of the galaxies’ centers and extents. We used the optical positions and inclinations of the galaxies, as well as the R_{HI} , H I recession velocities and rotation velocities shown in Table 5 as initial guesses in our fits, and did not fix any of the parameters at first. We limited the fit to R_{HI} for each galaxy. Most of the galaxies were well-fit using Brandt curves (Brandt 1960). In the case of SDSS0934+0014 and SDSS1319+5253B, neither a Brandt curve nor an exponential fit produced rotation velocities that were smaller than the uncertainties on the velocities. These galaxies are flagged in Table 6. We did not use other rotation curve models, such as tilted-ring fits, due to the limited spatial resolution of our maps. Two of the galaxies, SDSS1402+0955 and SDSS1507+5511, were not well-fit without fixing the central positions of their rotation curves to the positions of their optical centers. It is possible that the poor fits were due to limited spatial resolution (as LCBGs are spatially compact, even the higher-resolution moment maps that we produce have only a handful of beams across the major axis), or spectral channels that are too broad to provide a sufficient number of velocity data points to fit for galaxies that are slowly rotating or face-on. It is also difficult to distinguish between a galaxy with an intrinsically low V_{rot} and one that has a higher intrinsic V_{rot} but is face-on, so uncertainty in a galaxy’s inclination can lead to

large uncertainties in V_{rot} . Since we do not have enough resolution elements, both spatially and spectrally, to fit more detailed tilted-ring rotation models to decompose the LCBGs into multiple gas components, we simply report their V_{rot} values as calculated and emphasize that all LCBGs in our sample show clear signs of ordered rotation. The results of rotation curve fitting are listed in Table 6, and the rotation curves that we fit are plotted in Figure 12. The V_{rot} values derived from measuring along the major axis of each galaxy are less dependent on models that have systematic uncertainties than rotation curve fits, and are more easily reproduced. Thus, we use the velocities along the major axis shown in Table 5 when discussing V_{rot} in the remainder of the paper.

3.4. Comparison with single-dish results

One of the primary goals of this study was to investigate how results from single-dish observations of nearby LCBGs compare to those derived from resolved maps. Since LCBGs are unresolved at the distances at which they are common, it is important to determine whether unresolved observations of these galaxies are sufficient to describe their global properties and predict their evolutionary paths. Seven of the LCBGs in our sample were observed with the GBT by Garland et al. (2004) at a resolution of $\sim 9'$, which is large with respect to their R_{HI} . We compare the M_{HI} of these galaxies derived from our resolved observations and the unresolved observations of Garland et al. (2004) in the last column of Table 4. We find that for six of the eight LCBGs common to both samples, the single dish observations generate a larger M_{HI} than what we calculate from resolved observations. We recover more H I emission for two of the LCBGs in our sample (SDSS0728+3532 and SDSS1319+5203) than was measured by Garland et al. (2004), which is likely due to those galaxies residing in H I envelopes that include other galaxies (the H I masses we report for those two LCBGs are for the entire envelope), though their H I envelopes are unresolved with the GBT beam. On average, the M_{HI} that we measure is 76% of what Garland et al. (2004) measured in their single dish observations, although there is a large dispersion between the values obtained in both measurements. In comparison, in resolved observations of five LCBGs with the VLA, Garland et al. (2007) measured values of M_{HI} that were on average 61% of the measured single dish values from Garland et al. (2004), with a similarly large dispersion. If we remove the two galaxies that reside in larger H I envelopes from consideration, we recover on average 58% of the M_{HI} that Garland et al. (2004) measured for the remaining six galaxies, with a dispersion of 24%, which is consistent with the Garland et al. (2007) result.

We also compare the V_{rot} and M_{dyn} values we derive from our velocity fields to those calculated from W_{20} corrected for inclination in the Garland et al. (2004) sample in Table 7 (SDSS0125+0110 is left out of this discussion because it was not observed by Garland et al. 2004). With the exception of SDSS1507+5511, the single-dish V_{rot} values calculated by Garland et al. (2004) using half of W_{20} corrected for inclination are larger than the V_{rot} values that we measure using a cut along the major axis ($\langle 0.5 \times W_{20}/V_{\text{rot}} \rangle = 2.6 \pm 1.6$). Since the observations of Garland et al. (2004) were made with beam sizes large enough to include contributions from companion galaxies in the case of

SDSS0119+1452, SDSS0934+0014, SDSS0936+0106, SDSS1319+5203, and SDSS1402+0955, and tidal features in the case of SDSS0728+3532 and SDSS1319+5203, their measurements of W_{20} are not spatially resolved enough to distinguish the velocity contributions of the LCBGs from the contributions of their nearby companions.

When calculating M_{dyn} , Garland et al. (2004) estimated that $R_{\text{HI}} = 2 \times R_{25}$, following Broeils & van Woerden (1994), since they did not have measured values of R_{HI} . We compare the estimated and measured values of R_{HI} in Table 7. The R_{HI} values that we measure are on average 84% of those used in Garland et al. (2004), though the scatter is relatively large ($\langle R_{\text{HI}}^{\text{GMRT}} / R_{\text{HI}}^{\text{est.}} \rangle = 0.84 \pm 0.40$). SDSS0728+3532, SDSS0936+0106, and SDSS1319+5203 have measured R_{HI} values that are larger than those that Garland et al. (2004) estimated. We use our measured R_{HI} to calculate M_{dyn} here.

With the exception of SDSS0936+0106 and SDSS1507+5511, the M_{dyn} within the estimated R_{HI} calculated by Garland et al. (2004) are larger than those that we calculate here, owing to the larger V_{rot} and R_{HI} values estimated using single dish observations. On average, the single-dish M_{dyn} values are 10.3 times larger than M_{dyn} measured along the galaxies’ major axes, with a large scatter ($\sigma_{M_{\text{dyn}}^{\text{GBT}}/M_{\text{dyn}}^{\text{GMRT}}} = 10.9$). We note that we used slightly different distances to calculate M_{dyn} than Garland et al. (2004) did. The recession velocities we measured, and thus the distances we calculated, were on average 8 km s^{-1} lower than those measured by Garland et al. (2004). As this translates to a difference of 0.1 Mpc, and no galaxy had a difference of more than 1 Mpc, we do not consider differences in our recession velocity measurements to be a significant source of error in our comparison.

The H I mass fractions, $f_{\text{gas}} = M_{\text{HI}}/M_{\text{dyn}}$, that we calculate using our resolved observations are on average nine times larger than those calculated from single-dish measurements, though with nearly as large of a standard deviation ($\langle f_{\text{gas}}^{\text{GMRT}} / f_{\text{gas}}^{\text{GBT}} \rangle = 9.0 \pm 8.9$). Only SDSS0936+0106 and SDSS1507+5511 have smaller f_{gas} when using resolved data than the f_{gas} values derived from single-dish observations. For two of the LCBGs, SDSS0728+3532 and SDSS1319+5203, the M_{HI} values that we calculate encompass the entire, multi-galaxy H I envelopes in which these galaxies reside, while M_{dyn} only encompasses the LCBGs. As a result, the f_{gas} that we calculate are likely much higher than the true values (for example the f_{gas} values of SDSS1319+5203 and Mrk 325 are 5.0 and 1.7, respectively, which are unrealistically high).

The major advantages that our current study have over those undertaken with single dishes are that (1) our improved spatial resolution enables us to distinguish individual galaxies from their nearby companions, (2) mapping the galaxies allows for their rotation axes to be identified and their V_{rot} to be measured rather than estimated from linewidths, and (3) mapping the galaxies also makes measuring their R_{HI} possible, enabling calculations of their M_{dyn} to be made with fewer assumptions. We generally calculate lower M_{dyn} and higher f_{gas} than what was calculated from single-dish measurements by Garland et al. (2004). This result strengthens their assertion that LCBGs are gas-rich galaxies with smaller M_{dyn} than elliptical galaxies. We note that the V_{rot} , and thus M_{dyn} , that we calculate depend on the galaxies’ inclinations. Since we do not have the spatial

or velocity resolution to reliably fit rotation curves and inclination models to the LCBGs in our sample, we have not been able to accurately measure the inclinations of the galaxies’ gas. We are thus restricted to the same assumption that Garland et al. (2004) made: the gas in these galaxies is inclined at the same angle with respect to our line of sight as their optical components. Thus, even though our resolved study better measures the gas properties of each LCBG, it is still limited by uncertain galaxy inclinations. Our results are consistent with the conclusions of Garland et al. (2004) that LCBGs are gas-rich and morphologically heterogeneous.

From comparing the H I properties of the LCBGs in our sample to those measured with a single dish, we find that the V_{rot} , R_{HI} , and M_{dyn} that we measure are not related by a simple scale factor to those estimated using single dish linewidths and R_{25} . See Figure 13 for a visual representation of the scatter in the H I properties that we measure when compared to those reported by Garland et al. (2004). We note that our sample size is small, so we cannot rule out a characteristic relationship between R_{25} and R_{HI} or between single-dish linewidths and V_{rot} in LCBGs, though we do not find such a relationship here.

3.4.1. Comparison with stellar masses

As a constraint on the M_{dyn} that we have calculated, we have also calculated stellar masses, M_* , for each LCBG using the equation $\log(M_*/L) = a_\lambda + b_\lambda \times \text{Color}$ given in Bell & de Jong (2001), where a_λ and b_λ are constants dependent on the wavelength of measured luminosity and are tabulated in Table 1 of Bell & de Jong (2001). We used the $B - V$ colors and B-band absolute magnitudes calculated from SDSS magnitudes that we listed in Table 1. We note that two LCBGs, SDSS0934+0014 and Mrk 325, had M_{dyn} values lower than their stellar masses. Bell & de Jong (2001) state that the scatter on their color - M_*/L relation is $\sim 10\%$, which is smaller than the difference between the M_* and M_{dyn} values for these galaxies, so it is not likely that uncertainties on the color - M_*/L relation are responsible for this unphysical result. There are two possible reasons for these two galaxies having larger M_* than M_{dyn} . First, if a galaxy is more face-on than the inclination given in Hyperleda, then we have likely underestimated its M_{dyn} due to under-correcting its rotation velocity for inclination. Since these two galaxies were the most difficult to identify axes of rotation for, it is likely that the uncertainty in their rotation velocities is higher than for the other LCBGs. Second, the equation used to calculate M_* is a relationship between M_*/L and galaxy colors determined by a model for several combinations of colors and optical and near-infrared absolute magnitudes. As was shown in Garland et al. (2004), LCBGs are more likely to have lower M/L than the average for local galaxies, and Bell & de Jong (2001) find that bluer colors correlate with lower M/L . If LCBGs significantly deviate from the color- M/L relationship that Bell & de Jong (2001) have derived (for example, if the $B - V$ that we use in our calculations is redder than the average $B - V$ for a galaxy’s disk), we may be overestimating their stellar masses.

3.5. Tully-Fisher relation

The Tully-Fisher (T-F) relation (Tully & Fisher 1977) posits that for rotating galaxies, intrinsic luminosity is proportional to the galaxy’s V_{rot} raised to the fourth power. Garland et al. (2004) showed that not all of the LCBGs in their sample follow the T-F relation when they estimated V_{rot} using single-dish linewidths. It would be expected that a star-forming galaxy’s intrinsic brightness would temporarily be elevated with respect to the brightness associated with its V_{rot} on the T-F relation, and Garland et al. (2004) did see some evidence of that effect in their sample. However, they also found that some LCBGs are less intrinsically bright than their V_{rot} would suggest, which would not be expected for star-forming galaxies. Since a galaxy undergoing active star formation becomes less intrinsically bright once its star-forming episode ends, an LCBG that is fainter than would be expected for a galaxy on the T-F relation would never become bright enough to evolve onto the T-F relation. However, if a galaxy’s V_{rot} is overestimated by its single-dish linewidth, the galaxy could appear to be too faint to follow the T-F relation given its (overestimated) V_{rot} . This scenario could happen if, for example, an unresolved nearby companion or tidal feature exists whose recession velocity overlaps with the rotation velocity range of the target galaxy. For example, Garland et al. (2004) found that six of the ten LCBGs in their sample that are too faint to follow the T-F relation have companions. Since our resolved observations enable us to measure the V_{rot} values of the LCBGs in our sample, we revisit whether LCBGs follow the T-F relation using our velocity measurements.

We have plotted the LCBGs in our sample in Figure 14 along a version of the T-F relation described in Tully & Pierce (2000). In this plot, we use V_{rot} as measured along the galaxies’ major axes and corrected for optical inclination, as well as their M_B listed in Table 1. We also plotted the corresponding linewidths and M_B calculated for those LCBGs in Garland et al. (2004), with the exception of SDSS0125+0110 as it was not observed in that study. Five of the nine LCBGs in our sample appear to follow the T-F relation (within error bars), while four LCBGs are brighter than anticipated given their V_{rot} . None of the LCBGs in our sample have lower than expected luminosities given their V_{rot} values, while six of the LCBGs have low luminosities with respect to rotation velocities inferred from their linewidths as measured in Garland et al. (2004). Since the average V_{rot} derived from half of the galaxies’ single-dish linewidths is nearly three times the V_{rot} values that we measure, we can infer that the cause of some LCBGs appearing to not be able to follow the T-F relation is likely due to uncertainties in estimating V_{rot} from single-dish linewidths.

In addition to a temporarily elevated luminosity due to ongoing star formation, one potential cause of some LCBGs’ deviation from the T-F relation could be disturbed H I velocity fields due to mergers or interactions. Eight of the nine LCBGs in our sample have nearby companions or show signs of disturbed gas morphology, though their optical morphologies remain disk-like. If a galaxy’s V_{rot} is not accurately measured by taking a cut along its major axis (but is instead underestimated), the galaxy could appear to be too luminous for its measured V_{rot} . We also note that our measured V_{rot} values include a correction for optical inclination. If a galaxy’s gas disk inclination differs from the measured optical inclination, a systematic error will occur in their corrected values of V_{rot} that

we do not account for in our measurements.

Another possible cause of deviation from the T-F relation, which does not exclude a merger scenario, could be due to the formation of a bulge or pseudobulge (Tonini et al. 2014). If LCBGs are undergoing their final major burst of star formation while they build a bulge and transition to more quiescent S0 or dE-type galaxies, we may be able to see evidence of this transformation in their H I properties. Earlier-type spiral galaxies have higher mass-to-light ratios than later-type spirals, so their T-F relations tend to be flatter than the average T-F relation for spiral galaxies (Tonini et al. 2014). None of the LCBGs in our sample appear to have higher mass to light ratios than the T-F relation would suggest (see Figure 14), so we do not see evidence that the LCBGs in our sample have prominent bulges like Sa-type galaxies.

As the LCBGs in our sample either follow the T-F relation or have the potential to evolve onto it once their blue luminosities fade due to decreased star formation activity, we can infer that the LCBGs in our sample are likely to be rotation-supported. An additional consideration to include in our analysis is the effect of velocity dispersion on the galaxies’ rotation velocities. Since we measured the LCBGs’ rotation velocities at the edges of the extent of the galaxies’ H I, where their velocity dispersions are relatively low (see the Moment 2 maps in Figures 1 - 9), the effects of velocity dispersions on the galaxies’ rotation velocities are likely to be small. It is possible that the rotation velocities measured by Garland et al. (2004) from single-dish linewidths could be affected by the inclusion of velocity dispersion. If this is the case, the additional contribution from velocity dispersion would increase the measured linewidth relative to what would be measured due to pure rotation. This increase could contribute to the data points in Figure 14 from Garland et al. (2004) that lie to the right of the T-F relation, where it is impossible to evolve onto the T-F relation solely due to quenching of star formation. We discuss velocity dispersions further in Section 3.6.

3.6. Velocity dispersions

We calculated the average intensity-weighted velocity dispersions, σ , of the LCBGs in our sample by taking the average pixel values of the Moment 2 maps at four locations: (1) within a circle bordered by the half-light radius, $R_{\text{eff}}(\text{B})$, (2) within a circle bordered by R_{25} , (3) for the whole disk within R_{HI} , and (4) outside of region within R_{25} . We chose the R_{25} radius limit because it generally signifies the outer limit of active star formation (Tamburro et al. 2009). Thus, σ within R_{25} is a measure of the gas properties that affect and are affected by galaxies’ star formation, while σ outside of R_{25} probes the kinematics of the galaxies beyond the region where they actively form stars. These values of σ are tabulated in Table 8.

We find that the areas of highest σ tend to coincide with the optical centers of the LCBGs in our sample, similar to what Tamburro et al. (2009) measured for spiral galaxies. This is true not only for the relatively isolated LCBGs, but also for LCBGs with companions (even those with companions in a common H I envelope, with obvious evidence of gas interactions and disturbed

morphology).

We also calculated the ratio of each LCBG’s V_{rot} (corrected for inclination) at a given radius to its average σ inside of that radius, $V_{\text{rot}}\sigma^{-1}$, to determine the relative contributions of ordered rotation and disordered motion of each galaxy’s H I emission. A galaxy’s $V_{\text{rot}}\sigma^{-1}$ values are indicative of whether it has bulge-like or disk-like behavior, with values of $V_{\text{rot}}\sigma^{-1} < 1$ signifying that random motions of the gas dominate over rotation. Such values of $V_{\text{rot}}\sigma^{-1}$ are typically present in a galaxy’s bulge, if it has one, while values of $V_{\text{rot}}\sigma^{-1} \sim 1$ can be found in “pseudobulges”, which are built up by internal processes and maintain some rotation (for a review, see Kormendy & Kennicutt 2004). We also wanted to investigate possible gravitational instabilities in the disks as a potential trigger for star formation, which can be traced by comparing $V_{\text{rot}}\sigma^{-1}$ to the amount of gas available in the disk.

Another implication of centrally-peaked σ values is that the outer parts of the galaxies’ disks have relatively low σ , which is a property associated with gas that is less dynamically hot. All nine of the LCBGs in our sample have V_{rot} values in excess of their σ values when measured at R_{HI} . In Table 8, we show values of $V_{\text{rot}}\sigma^{-1}$ within several radii. We find that $V_{\text{rot}}\sigma^{-1}$ increases at larger radii, with the highest values occurring when σ is measured outside of R_{25} , and the lowest values occurring within R_{eff} .

One way we can infer whether LCBGs are dominated by bulges is to compare their ratios of ordered to disordered motion to their ellipticity, ϵ . Using virial theorem arguments, $V_{\text{rot}}\sigma^{-1}$ can be related to ϵ by

$$\frac{V_{\text{max}}}{\sigma} = \frac{\pi}{4} \sqrt{2[(1 - \epsilon)^{-0.9} - 1]} \quad (4)$$

where $\epsilon = 1 - b/a$ (Sparke & Gallagher 2007). We plot this relation, which indicates the maximum ratio of ordered motions to random motions allowable for a given flatness of elliptical galaxies, in Figure 15. When measured within R_{25} , all of the LCBGs in our sample except one (SDSS0934+0014) lie above this relation, along with spiral galaxies and late-type dwarf galaxies from the THINGS sample (Walter et al. 2008), which shows that they rotate faster (or have smaller values of σ) than is permitted for elliptical galaxies. By contrast, all of the dwarf elliptical galaxies with a significant rotation component studied by Geha et al. (2003), and most of the dwarf ellipticals studied by van Zee et al. (2004), lie below this relation. When we measured V_{rot} at R_{eff} and the average σ within R_{eff} , the $V_{\text{rot}}\sigma^{-1}$ values of the galaxies in our sample lie near the relation, which implies that LCBGs have approximately the maximum V_{rot} possible for elliptical galaxies in their most central areas. Bershadsky et al. (2005) show that a sample of very blue ($B - V \sim 0.25$), very compact ($S_{\text{Be}}(B) \sim 19 \text{ mag arcsec}^{-2}$) intermediate-redshift LCBGs lie below the relation (see their Figure 2), which suggested to them that LCBGs may evolve into dwarf elliptical galaxies once their star formation has been quenched. That study differs from ours in that it surveyed an extreme subset of intermediate-redshift LCBGs and measured ionized gas rather than H I. Pérez-Gallego et al. (2011) measured $V_{\text{rot}}\sigma^{-1}$ for ionized gas using optical emission lines for a sample of local LCBGs that has

two galaxies in common with our sample (SDSS1507+5511 and Mrk 325). When compared with the ellipticities of those galaxies, the LCBGs in their sample behave in a way similar to the LCBGs in our sample measured at R_{eff} . The $V_{\text{rot}}\sigma^{-1}$ values that we have measured make the presence of large-scale classical bulges that contain gas unlikely at present in LCBGs, though the gas in the innermost regions of LCBGs may display bulge-like behavior. This suggests that if the local LCBGs in our sample are representative of the population of LCBGs that is common at $z \sim 1$, those higher-redshift LCBGs must also be dominated by ordered rotation. If this was the case, then LCBGs at higher redshifts are likely disk galaxies with extensive star formation in their disks, rather than irregular or spheroidal galaxies.

3.6.1. Building bulges

An alternative scenario to star formation triggered by mergers or interactions with companions is the hypothesis that LCBGs are bright, star-forming bulges (or bulge progenitors) of disk galaxies (Barton & van Zee 2001; Hammer et al. 2001). This scenario is consistent with the centrally-peaked σ values and relatively low central $V_{\text{rot}}\sigma^{-1}$ values that we find for many of the LCBGs in our sample. However, the $V_{\text{rot}}\sigma^{-1}$ values we observe across the whole radii of LCBGs are not low enough for the LCBGs in our sample to be “classical” bulges which, like elliptical galaxies, are not typically rotation-supported and have $V_{\text{rot}}\sigma^{-1} < 1$ (Kormendy & Kennicutt 2004). The motion of the gas in the galaxies in our sample is dominated by rotation ($V_{\text{rot}}\sigma^{-1} > 1$) even within R_{25} , and even for the LCBGs with disturbed velocity fields, so we rule out the existence of gas-rich “classical” bulges in our sample. It is possible that the LCBGs in our sample have or are developing bars or “pseudobulges” (Kormendy & Kennicutt 2004), which are less supported by random motions than they are by rotation.

Along these lines, it is possible that LCBGs are developing “clump-origin bulges” (e.g. Noguchi 1998, 1999, 2000, 2001; Dekel et al. 2009; Elmegreen et al. 2009; Inoue & Saitoh 2012). In this scenario, gas infalling onto a galaxy’s disk develops overdensities within the disk that contract and become star-forming clumps. As the clumps orbit along with the rest of the disk, they move toward the center of the galaxy due to dynamical friction and can merge with other clumps. When these clumps merge with each other, star formation rates in the clumps increase briefly, which gives the clumps a bright, blue appearance and drives up the galaxies’ global star formation rates. Finally, the few large clumps that remain merge in the center of the galaxy, causing either a small clump-origin nuclear bulge or bar that maintains some of the the angular momentum that the clumps had in the disk. At this point, the star formation rate of the clumps rapidly declines (for a visual illustration of this process, see Figure 1 of Inoue & Saitoh 2012). The lifetimes of the clumps are governed by their size (more massive clumps are less likely to disperse due to outward pressure from their star formation), as well as their distance from the center of the galaxy (clumps that have less distance to travel as they move toward the center are more likely to reach the center of the galaxy intact). Clumpy galaxies have been observed at a range of redshifts, including galaxies that resemble

LCBGs. For example, Overzier et al. (2009) found that star-forming clumps, including large, bright central clumps, are common in a sample of Lyman Break Analog galaxies at $z \sim 0.1 - 0.3$ that have similar effective radii and dynamical masses to the LCBGs in our sample, and Garland et al. (2014) found that 40% of local LCBGs are clumpy, likely due to the buildup of accreted gas from interactions with companions or material in galaxy clusters.

To determine whether conditions in the LCBGs’ disks are conducive to the formation of clumps, we can use the gas properties we measure to calculate the galaxies’ Toomre parameters (Toomre 1964) for the stability of their disks’ gas:

$$Q_{\text{gas}} = \frac{\sigma \kappa}{\pi G \Sigma_{\text{gas}}} \quad (5)$$

where $\kappa = \sqrt{2}V_{\text{rot}}R^{-1}$ for a flat rotation curve, and Σ_{gas} is the gas mass surface density. For a disk to be stable, $Q \gtrsim 1$. More accurate measures of Q incorporate the disks’ stellar components as well (Dekel et al. 2009), though we limit our present analysis to the LCBGs’ H I. In general, incorporating a stellar component will increase a galaxy’s value of Q .

Keeping in mind that a galaxy’s total mass is represented by $M_{\text{dyn}} = V_{\text{rot}}^2 R/G$, we can rearrange the above inequality for $Q > 1$ so that it highlights the criterion for disk stability in terms of gas properties we can measure:

$$\frac{V_{\text{rot}}}{\sigma_{\text{gas}}} < \frac{\sqrt{2}\Sigma_{\text{total}}}{\Sigma_{\text{gas}}}. \quad (6)$$

where Σ_{total} is the galaxy’s total surface mass density, which is calculated using its M_{dyn} within a given radius ($\Sigma_{\text{total}} = M_{\text{dyn}}/\pi R^2$). We note that for this discussion, we make the approximation that $f_{\text{gas}} = f_{\text{HI}}$. We plot the measured values at several radii for each of the LCBGs in our sample (excluding SDSS0728+3532 and SDSS1319+5253B, which are contained within a larger H I envelope) in Figure 16. All of the LCBGs in our sample except Mrk 325 have stable gas disks with respect to perturbations over a range of radii (for $Q < 1$, data points would lie above the curve in Figure 16, and for $Q > 1$, data points lie below the curve), which means that their f_{gas} would need to be higher for their disks to be unstable given their present values of $V_{\text{rot}}\sigma^{-1}$. Two of the LCBGs in our sample (SDSS0934+0014 and SDSS1402+0955) have the potential for local instabilities to form at large radii, and other LCBGs are within error bars of having $Q \lesssim 1$, though the uncertainties on their values of $V_{\text{rot}}\sigma^{-1}$ are large. Mrk 325 has the potential for local instabilities at all radii, though we note that we find $f_{\text{gas}} > 1$ for this galaxy, which is an unrealistic value (if we instead say that $f_{\text{gas}} = M_{\text{HI}}/(M_{\text{HI}} + M_*)$, Mrk 325 is mostly stable accross its disk). We note that we assume that f_{gas} is constant at all radii, which is unlikely to be the case given that the LCBGs’ H I emission is centrally concentrated. In addition, our assumption that $f_{\text{gas}} = f_{\text{HI}}$ is only a first-order approximation as the contribution to the gas mass from molecular gas is likely non-negligible. These effects would result in smaller $\Sigma_{\text{total}}/\Sigma_{\text{gas}}$ at all radii than what we assume, particularly at smaller

radii, which would bias Equation 6 toward a greater likelihood of disk instabilities at smaller radii than what we plot in Figure 16 (lower-radii data points will move to the left in Figure 16 if f_{gas} increases with decreasing radius).

In a study modeling gas infall onto galaxies, Dekel et al. (2009) found that if the cold gas streams that are feeding infall onto the disk are clumpy, the clumps more easily merge toward the center of the galaxy and form a spheroid shape, keeping the disk’s average $f_{\text{gas}} < 0.3$. In this scenario, the disk is usually stable. They found that conversely, if the streams are smooth, the disk can support clumps for a longer period of time. Noguchi (2000) found that requiring the local gas density to rise above a certain threshold before star-forming clumps could form yielded simulations consistent with observations of early- and late- type disks, and that for smaller galaxies, clumps may not be able to form at all and instead the infalling gas is fed into the center of the galaxy to form a bar. To estimate the likelihood of these scenarios, we can compare the M_{HI} values that we measure for the LCBGs in our sample to the clump masses that have been observed and modeled in other studies. Elmegreen et al. (2009) found that for spiral galaxies, each clump contains an average of 0.3% of its galaxy’s stellar mass, while for clump cluster galaxies (galaxies dominated by several bright clumps) each clump contains about 2% of the galaxy’s stellar mass. If we make the assumption that these ratios are also approximately valid for M_{HI} , we can multiply these percentages by the average M_{HI} of the LCBGs in our sample to find the expected clump masses. On average, a clump would contain about $1 \times 10^7 M_{\odot}$ of H I in a spiral LCBG, or about $7 \times 10^7 M_{\odot}$ of H I in a clump cluster LCBG. Noguchi (2000) found that in simulations, clumps were more likely to survive migration toward the galaxies’ centers in galaxies with clumps larger than $\sim 10^7 M_{\odot}$, while in galaxies with smaller clumps, the clumps were more likely to be disrupted and instead form a short bar from their gas. Though we do not have the sensitivity in our current study to measure the masses of gas clumps, nor the resolution to measure local overdensities in the LCBGs in our sample, future studies at higher resolutions may be able to identify density variations in LCBGs’ disks and determine the likely course of future evolution of the galaxies’ clumps. As both low-redshift LCBGs and their high-redshift analogs are often clumpy, further understanding of this phenomenon will be useful in predicting these galaxies’ evolutionary paths.

To determine whether any star-forming clumps due to gravitational instabilities in LCBGs are detectable over long timescales, we calculated the inspiral time for clumps, $t_{\text{ins}} = (V_{\text{rot}}\sigma^{-1})^2 \times t_{\text{dyn}}$, where $t_{\text{dyn}} = R_{\text{HI}}/V_{\text{rot}}$ (see, for example, Dekel et al. 2009; Genzel et al. 2014) using V_{rot} measured at R_{HI} and the average σ measured within R_{HI} for each LCBG. For the LCBGs in our sample, t_{ins} is longer than 1 Gyr (approximately the lifetime of a $\sim 2.5 M_{\odot}$, or late-B to early A-type star; Harmanec 1988; Maeder & Meynet 1989; Romano et al. 2005) for all but two LCBGs. This implies that if clumps can form in LCBGs, they can persist for several Gyr before they finally sink to LCBGs’ centers if they are not disrupted. When compared with less compact and less dynamically hot disk galaxies, however, the expected t_{ins} for LCBGs is relatively short. Since disk galaxies tend to have higher values of $V_{\text{rot}}\sigma^{-1}$ at lower redshifts than at higher redshifts (Kassin et al. 2012), the appearances of clumpy galaxies at $z \sim 1$ may evolve more rapidly than most disk galaxies with

star-forming clumps in the local universe due to their lower t_{ins} . Thus, since local LCBGs have relatively high values of $V_{\text{rot}}\sigma^{-1}$ and compact R_{HI} , their t_{ins} are likely more comparable to those of LCBGs at higher redshifts. Future resolved observations of LCBGs will help better measure local velocity dispersions and disk inclinations, which will better constrain inspiral times for clumps in their disks. In addition, resolving individual clumps and measuring their properties will determine whether feedback within the clumps due to radiation pressure will disperse the clumps on shorter timescales than t_{ins} .

3.7. Comparison with higher-redshift galaxies

Förster Schreiber et al. (2009) measured H_α velocity maps for a sample of $z \sim 2$ star-forming galaxies from the Spectroscopic Imaging survey in the Near-Infrared with SINFONI (SINS) survey. Most of the galaxies in their sample had clumpy H_α morphologies. They found that the galaxies in their sample fell into three groups based on their kinematics, with approximately a third of their sample falling into each category: rotation-dominated disks, compact dispersion-dominated galaxies, and merging systems. The H I velocity fields of the LCBGs in our sample resemble the H_α velocity fields of the rotation-supported galaxies in their sample, as shown in Figure 17 of Förster Schreiber et al. (2009). The LCBGs in our sample do not appear to be similar to star-forming galaxies supported by disordered motions; the dispersion-dominated galaxies in the Förster Schreiber et al. (2009) sample do not show a clear axis of rotation, while even the least rotationally-supported LCBGs in our sample show a clear velocity gradient.

Genzel et al. (2014) found that for a sample of 19 rotationally-supported, star-forming disk galaxies from the SINS survey with smooth velocity gradients and centrally-peaked velocity dispersions at $z \sim 2$, Q is also centrally-peaked. We can see from Figure 16 that this is true for the LCBGs in our sample as well. The solid line in Figure 16 represents $Q = 1$, with values of Q increasing to the bottom right. We see that for the LCBGs in our sample, the measurements at the smallest radii have larger values of Q than at larger radii. As mentioned in Section 3.6.1, we assume in Figure 16 that Σ_{gas} is constant at all radii, which is unlikely to be true since the H I emission in the LCBGs in our sample is centrally-peaked. If Σ_{gas} increases with decreasing radius in the LCBGs in our sample, then Q will not be as centrally-peaked as is implied by Figure 16. Genzel et al. (2014) argue that increased values of Q in the centers of galaxies could lead to the formation of a central bulge and the quenching of star formation where $Q > 1$. While our measurements of rotation velocities, velocity dispersions, and gas masses suggest that a similar central bulge is possible in the LCBGs in our sample, higher-resolution measurements of H I are needed for these galaxies to more conclusively identify central bulges that could lead to the quenching of star formation in LCBGs.

4. Conclusions

In this study, we have measured the H I properties of nine LCBGs from resolved maps. We conclude that

- The LCBGs in our sample are rotating disk galaxies with centrally-concentrated H I intensities and velocity dispersions;
- The H I linewidths measured for these galaxies by single dishes tend to overestimate their rotation velocities, likely due to the inclusion of companions or tidal features in the beam;
- The LCBGs in our sample have values of $V_{\text{rot}}\sigma^{-1}$ that are consistent with disk galaxies rather than dwarf elliptical galaxies when measured at R_{HI} and R_{25} , though some LCBGs have $V_{\text{rot}}\sigma^{-1}$ within R_{eff} that are consistent with bulgelike behavior; and
- The disks of the LCBGs in our sample are stable on average with respect to local perturbations, though they have the potential to form local instabilities at large radii.

We have found that the LCBGs exhibit a variety of gas morphologies, from regular, symmetric rotation to asymmetric, disturbed rotation to multiple galaxies in a common H I envelope. All of the LCBGs in our sample appear to be dominated by rotation at large radii ($V_{\text{rot}}\sigma^{-1}(R_{\text{HI}}) > 1$), and have significant rotation components at smaller radii. We do not have the resolution to robustly fit the inclinations of their disks, so their inclinations, and thus their corrected V_{rot} and values of $V_{\text{rot}}\sigma^{-1}$, are highly uncertain. We do not have enough information to comment extensively on the shapes of LCBGs’ rotation curves (or their mass distributions), though we have taken cuts along their major axes that display the shapes of their velocity profiles. The LCBGs in our sample tend to have asymmetric velocity profiles, which supports a scenario where LCBG star formation is the result of gas disturbance. We cannot conclusively distinguish whether this disturbance is externally or internally triggered, but the presence of companions near most of the LCBGs in our sample are not inconsistent with external mechanisms. Even so, even the most disturbed LCBGs tend to have identifiable H I rotation axes.

When compared to previous single-dish results (Garland et al. 2004), we measure lower values of V_{rot} for all of the LCBGs in our sample except for SDSS1507+5511. Six of the nine LCBGs have smaller measured R_{HI} values than what was estimated for them using $R_{\text{HI}} \sim 2 \times R_{25}(\text{B})$ (two of the exceptions, SDSS0728+3532 and SDSS1319+5203, have H I envelopes that include other galaxies, while the other exception, SDSS0936+0106, has a measured R_{HI} that is only 6% larger than its estimated R_{HI}). These discrepancies tend to result in smaller values of M_{dyn} , and larger values of f_{gas} , for LCBGs than those calculated from single dish measurements.

Though most of them have disturbed kinematics, the LCBGs in our sample do not appear to be exclusively the result of mergers. Seven (78%) of them have companions at comparable systemic velocities, and two (22%) of them have other galaxies within their H I envelopes. This implies

that the star formation in LCBGs is not required to be solely externally-triggered. Instead, some LCBGs’ star formation may be the result of intrinsic bulge-building, which could be enhanced by interactions but does not require interactions to proceed (we note, for example, that for the two LCBGs, SDSS0728+3532 and SDSS1319+5203, that are in three-galaxy interacting systems, only one of the galaxies in each system is an LCBG).

We found that the LCBGs in our sample either already follow the Tully-Fisher relation or have the potential to evolve onto it once their starbursts, and thus B-band luminosities, fade. While the LCBGs’ $V_{\text{rot}}\sigma^{-1}$ values look like those of dwarf elliptical galaxies at the smallest radii ($R < R_{\text{eff}}$), they resemble other types of spiral galaxies more closely at $R_{25}(\text{B})$. From this, we infer that the LCBGs in our sample are likely not dispersion-dominated bulges, and that they will not likely be able to passively evolve into dwarf ellipticals once their star formation is quenched. However, some of the LCBGs in our sample may be building small central bulges, as three of the galaxies have $V_{\text{rot}}\sigma^{-1}$ values at large radii ($R > R_{25}$) that are above the threshold of disk instability necessary for infalling gas to create star-forming clumps that may later merge to form a nucleus or bar.

The variety of optical and H I morphologies, environments and kinematics of the LCBGs in our sample lends support to the picture of LCBGs being a heterogeneous class of galaxies undergoing a common, short-lived evolutionary phase in their star formation histories. Since the LCBGs in our sample do not have common H I properties, we cannot predict a single future scenario for their evolution based on their gas morphologies. This is not surprising, as the relative abundance of LCBGs at $z \sim 1$ would suggest that, if LCBGs follow a single common evolutionary path, their end products would be similarly common in the local universe.

Since LCBGs appear to have such a variety of gas morphologies, future studies of their gas properties focusing on high-resolution mapping to further probe their internal dynamics, including the presence of star-forming gas clumps, bars, or bulges related to local gravitational instabilities, will better illustrate whether they have any common intrinsic star formation triggers. Such mapping would provide data useful for modeling LCBGs’ gas evolution to predict their timescales for future quenching of their star formation. We are studying the radio continuum properties of a larger local sample of LCBGs to calculate their current star formation rates. This information, coupled with LCBGs’ M_{HI} values, will help us understand whether LCBGs’ gas depletion timescales given their current star formation rates are shorter than their expected timescales for star formation quenching. This will provide better understanding for the evolutionary paths of this formerly common, currently rare, class of galaxies.

We thank the staff of the GMRT who have made these observations possible. GMRT is run by the National Centre for Radio Astrophysics of the Tata Institute of Fundamental Research.

The National Radio Astronomy Observatory is a facility of the National Science Foundation operated under cooperative agreement by Associated Universities, Inc.

This research has made use of the NASA/IPAC Extragalactic Database (NED) which is operated by the Jet Propulsion Laboratory, California Institute of Technology, under contract with

the National Aeronautics and Space Administration. We acknowledge the use of NASA’s SkyView facility (<http://skyview.gsfc.nasa.gov>) located at NASA Goddard Space Flight Center.

Funding for the SDSS and SDSS-II has been provided by the Alfred P. Sloan Foundation, the Participating Institutions, the National Science Foundation, the U.S. Department of Energy, the National Aeronautics and Space Administration, the Japanese Monbukagakusho, the Max Planck Society, and the Higher Education Funding Council for England. The SDSS Web Site is <http://www.sdss.org/>.

A. Individual Galaxies

A.1. SDSS0119+1452

SDSS0119+1452 (NGC 469) is a galaxy that shows rotation in its Moment 1 map (though it has a narrow linewidth), but also has an excess clump of H I off of its southwest corner (no similar feature appears in the SDSS optical images). Its axis of rotation in the Moment 1 map coincides with what appears to be the optical minor axis. Its optical morphology looks asymmetric, with a blue, clumpy center and no discernable spiral arms. Hyperleda classifies it as S0-Sa. NED identifies a companion (NGC 471) about $8'$ ($90 \times R_{\text{eff}}(\text{B})$) away that is visible in SDSS images but is not detected in our H I observations. At low resolutions, the gas clump is merged with the galaxy’s gas, but at higher resolutions it appears separate. It is possible that it is connected at a low column density level, but at high resolutions it does not overlap with the galaxy at even the 2σ level (~ 0.5 mJy/beam in the high-resolution data cube).

A.2. SDSS0125+0110

SDSS0125+0110 (ARK 044) is a rotating galaxy in the NGC 533 group. It has no nearby companions. It has the least-disturbed morphology of all of the galaxies in our sample, and a redder center than most of the other LCBGs discussed here. This galaxy was not in the original Garland et al. (2004) sample, and following the SDSS DR7 photometry, it does not fall within the LCBG criteria defined by Werk et al. (2004); it is slightly redder and less compact. Hyperleda classifies this galaxy as Sb.

A.3. SDSS0728+3532

SDSS0728+3532 (ARK 134) is a rotating galaxy with a large, low column density H I tidal tail extending to the south. The tail appears to be caused by an interaction with at least one other blue galaxy (SDSS0728+3531), which optically coincides with the location of the H I emission of the tail (though it does not have an obvious velocity component in the Moment 1 map distinct

from the tidal tail, so we cannot confirm that it is the cause of the tidal tail). More H I emission is detected to the west of SDSS0728+3532 in our observations, which coincides with another blue galaxy in SDSS images. There is no optical emission corresponding to the the tidal tail visible in SDSS images. Hyperleda classifies SDSS0728+3532 as an Sbc.

A.4. SDSS0934+0014

SDSS0934+0014 (UGC 05097) has a disturbed morphology and may be face-on, as its rotation curve is difficult to fit (though Hyperleda gives its optical inclination as 68°). It has a companion about $11'$ ($123 \times R_{\text{eff}}(\text{B})$) to the southeast, and also has a blue companion $1'$ ($11 \times R_{\text{eff}}(\text{B})$) to the north (UGC 05099) that is not detected in either the low-resolution or high-resolution maps. SDSS0934+0014 and its northern companion are not obviously interacting in the SDSS optical image, but SDSS0934+0014 shows much more disturbed rotation than its H I profile indicates, so interaction is possible. There is a steeper gradient in both velocity contours and velocity dispersion contours near the border of the two galaxies, which could also indicate that some interaction is taking place. The H I profile at the location of the interaction does appear to have multiple components. NED classifies SDSS0934+0014 as a pair of galaxies, with a faint elliptical galaxy also interacting with SDSS0934+0014 to the north. Hyperleda classifies SDSS0934+0014 as an Sa galaxy.

A.5. SDSS0936+0106

SDSS0936+0106 (CGCG 007-009), like SDSS0125+0110, is a non-disturbed, non-interacting rotating galaxy. Unlike SDSS0125+0110, SDSS0936+0106 does have a blue companion galaxy about $5'$ ($44 \times R_{\text{eff}}(\text{B})$) to the northwest. There does not seem to be any evidence of the two galaxies interacting from the H I moment maps. Its H I emission is centrally peaked, its rotation is ordered, and its velocity dispersion is higher at the center and lower at the edges. Hyperleda does not have a classification for SDSS0936+0106, though NED classifies it as Sb.

A.6. SDSS1319+5203

SDSS1319+5203 (SBS 1317+523B) is one of a trio of blue galaxies sharing a common H I envelope as seen at low resolution. The other two galaxies are not LCBGs. One, Mrk 251, is blue and compact, though it is too faint to be classified as an LCBG. The other, SBS 1317+523A, is blue and bright, but its surface brightness is too low to qualify for LCBG status. SBS 1317+523B is included in the Garland et al. (2004) sample, but all three galaxies are well within the $9'$ GBT beam, so contamination from both galaxies likely affects their measurements. Hyperleda classifies SBS 1317+523B as Sb-Sbc, and Mrk 251 as Sab. The galaxy group is dominated by SBS 1317+523A

and the velocity field for the system shows interaction between it and SBS 1317+523B.

A.7. SDSS1402+0955

SDSS1402+0955 (NGC 5414) is a bright, blue galaxy that does not appear to have any companions detected in H I, though in an SDSS image there appear to be several nearby galaxies in the plane of the sky. Its velocity field shows that it appears to be regularly rotating. Hyperleda classifies it as an elliptical galaxy in a multiple-galaxy system, though NED does not have a galaxy with velocity information at a similar velocity to SDSS1402+0955 within $5'$ of the LCBG. The SDSS optical image does appear asymmetrical, with a diffuse stellar halo that may show signatures of past interaction. The H I image shows a bit of asymmetry on the receding edge, so it is possible that a past interaction or merger could have upset the galaxy's rotation enough to make rotation curve fitting difficult, even if position-velocity plots look relatively undisturbed.

A.8. SDSS1507+5511

SDSS1507+5511 (UGC 09737) is a rotating galaxy with an excess of gas above its plane of rotation. It has a faint blue companion about $9'$ ($69 \times R_{\text{eff}}(\text{B})$) to the northeast (in the direction of the excess gas) that is detected in our H I observations. Hyperleda classifies UGC 09737 as a compact Sbc galaxy. Its H I emission is centrally peaked, with its peak coinciding with the optical emission of the galaxy. While its velocity field shows rotation, it is difficult to fit a rotation curve to this galaxy without large errors given the spatial resolution of our observations.

A.9. Mrk 325

Mrk 325 (NGC 7673) is a disturbed galaxy that has a companion, Mrk 326, that was observed in H I by Nordgren et al. (1997) and that we also detect in our H I observations. Pérez-Gallego et al. (2010) observed Mrk 325 in H α and found that, while it has an asymmetric, complex velocity field likely resulting from a minor merger, it is a rotating galaxy with a position angle of 168° and $V_{\text{rot}} = 30 \text{ km s}^{-1}$ before correcting for inclination. The minor merger may be with an infalling dwarf galaxy, which Pérez-Gallego et al. (2010) find has a separate kinematic component from the rest of Mrk 325. Garland et al. (2007) observed Mrk 325 in H I with the VLA in C configuration with a beam size of $\sim 20''$ and found that its emission is disturbed and shows a small velocity gradient. Our H I map, which combines the Garland et al. (2007) map with new B configuration data and archival D configuration maps from Nordgren et al. (1997), shows similar morphology and velocity information, and does not feature an obvious major axis of rotation. Nordgren et al. (1997) described Mrk 325 as a face-on galaxy with a possible warp. Hyperleda classifies Mrk 325 as an Sc.

Table 1. Optical properties

Source ^a	Common Name	D ^b (Mpc)	R _{eff} (B) ^c (kpc)	B − V ^d	m _B ^e	M _B ^f	SBe(B) ^g B Mag $''^{-2}$	Hubble Type ^h
SDSS J011932.94+145219.0	NGC 469	54.6	1.45	0.37	14.9	-18.8	20.5	S0/a
SDSS J012539.72+011041.0	ARK 044	80.4	2.37	0.62	15.5	-19.0	21.3	Sb
SDSS J072849.74+353255.2	ARK 134	58.6	1.41	0.41	14.7	-19.1	20.1	Sbc
SDSS J093410.62+001431.8	UGC 05097	75.8	1.97	0.46	14.2	-20.2	19.8	Sa
SDSS J093635.36+010659.7	CGCG 007-009	76.0	2.54	0.51	14.7	-19.7	20.8	Sb
SDSS J131949.94+520341.2	SBS1317+523B	69.9	1.16	0.30	15.5	-18.7	20.1	...
SDSS J140203.52+095545.5	NGC 5414	65.3	1.75	0.45	13.9	-20.2	19.6	E?
SDSS J150748.35+551108.7	UGC 09737	49.6	1.88	0.44	14.5	-19.0	20.9	Sbc
Mrk 325 ⁱ	NGC 7673	44.0	1.23	0.41	13.6	-19.6	19.4	Sc

^aSDSS source names are of the form SDSS JHHMMSS.SS+DDMMSS.S and are hereafter shortened to SDSS HHMM+DDMM.

^bDistances were taken from NED’s luminosity distances using $H_0 = 70 \text{ km s}^{-1} \text{ Mpc}^{-1}$.

^cHalf-light radii in the B band calculated using SDSS g and r Petrosian radii.

^dColors calculated from SDSS g and r magnitudes.

^eB-band apparent magnitudes calculated from SDSS g and r magnitudes.

^fB-band absolute magnitudes calculated from m_B and luminosity distances.

^gSurface brightnesses in the B band calculated from M_B , $R_{eff}(B)$, and luminosity distances.

^hFrom Hyperleda, except SDSS0936+0106 (from NED). SDSS1319+52303 does not have a Hubble type classification in Hyperleda or NED; Galaxy Zoo (Lintott et al. 2011) classifies this galaxy as “uncertain.”

ⁱMrk 325 is at the J2000 (RA, Dec) position (23:27:41.0, +23:35:21).

Table 2. Imaging parameters

Galaxy	High-res beam (arcsec ²)	Robustness	UV taper (k λ)	UV range (k λ)	# CLEAN iterations	Low-res beam (arcsec ²)	Robustness	UV taper (k λ)	UV range (k λ)	# CLEAN iterations
SDSS0119+1452	13×13	2	70×70	100	50	52×47	5	3×3	5	50
SDSS0125+0110	22×13	5	30×30	50	6000	54×45	5	3×3	5	35
SDSS0728+3532	13×8	5	70×70	100	180	55×53	5	3×3	5	60
SDSS0934+0014	20×20	5	30×30	40	200	75×49	5	3×3	5	25
SDSS0936+0106	12×11	3	70×70	100	100	55×46	5	3×3	5	950
SDSS1319+5203	15×12	5	30×30	50	400	63×50	5	3×3	5	50
SDSS1402+0955	23×14	2	30×30	50	6000	53×53	5	7×7	10	20
SDSS1507+5511	11×9	5	30×30	50	130	52×51	5	3×3	5	40
Mrk 325 ^a	6×6	0	50					

^aThe data cube for Mrk 325 is from a combination of B, C, and D configuration observations.

Table 3. Companion sources visible in maps

LCBG	Companion Name	RA (J2000)	Dec (J2000)	Separation (arcminutes)	Separation ^a (R _{eff} (B))	V _{sys} ^b (km s ⁻¹)	Detected?
SDSS0119+1452	NGC 471	01:19:59.6	+14:47:10	8.2	90	4137	N
SDSS0728+3532	GALEXASCJ072841.30+353206.1 ^c	07:28:41.3	+35:32:06	2.0	24	3930	Y
	SDSS072849.02+353124.6	07:28:49.0	+35:31:24	1.5	18	4010	Y
SDSS0934+0014	UGC05097 Notes01	09:34:10.5	+00:15:29	1.0	11	4665	N
	UGC 05099	09:34:34.2	+00:05:23	11	123	4954	Y
SDSS0936+0106	SDSS093626.68+011128.8	09:36:26.7	+01:11:28	5.0	44	4900	Y
SDSS1319+5203	SBS1317+520 ^d	13:19:46.2	+51:48:06	15.6	270	...	Y
	SBS1317+523A	13:19:47.5	+52:04:13	0.6	11	4588	Y
	Mrk 251	13:20:01.0	+52:03:03	1.8	32	4581	Y
SDSS1507+5511	SDSS150804.21+551954.0	15:08:04.2	+55:19:54	9.0	69	3385	Y
Mrk 325	Mrk 326	23:28:06.1	+23:31:52	6.7	70	3519	Y

^aProjected separation from target galaxy in multiples of the target galaxy's R_{eff}(B).

^bV_{sys} is approximated from moment maps if detected, or taken from NED if not detected.

^cSDSS classifies this object as a star; NED classifies it as a UV source.

^dNED classifies this object as a QSO at z = 1.06.

Table 4. LCBG H I Profile Properties

Galaxy	$V_{\text{sys}}^{\text{a}}$ (km s ⁻¹)	W_{20}^{b} (km s ⁻¹)	$\int \text{Sdv}$ (Jy km s ⁻¹)	M_{HI} (10 ⁹ M _⊙)	$\frac{M_{\text{HIGMRT}}^{\text{c}}}{M_{\text{HIGBT}}}$	Companion in GBT beam? ^d
SDSS0119+1452	4123	52.1	1.0	0.85	0.4	Y
SDSS0125+0110	5875	126.8	3.3	5.4
SDSS0728+3532 ^e	3962	166.1	9.8	7.4	1.2	N
SDSS0934+0014	4903	125.8	2.2	2.5	0.5	Y
SDSS0936+0106	4909	181.2	2.0	2.3	0.6	Y
SDSS1319+5203 ^e	4607	139.4	11.2	11.4	1.4	Y
SDSS1402+0955	4251	262.3	4.9	4.3	0.7	Y
SDSS1507+5511	3358	124.2	3.8	2.0	1.0	N
Mrk 325 ^f	3364	54.1	3.2	1.7	0.3	Y

^a V_{sys} is measured halfway between the channels used to measure W_{20} .

^b W_{20} is corrected for random motions following Equation 12 of Tully & Fouque (1985).

^c M_{HIGBT} values are taken from Garland et al. (2004).

^dTaken from Table 1 of Garland et al. (2004).

^eProperties listed are for the entire H I envelope, which contains multiple galaxies.

^fMeasurements are taken from the high-resolution cube. For data measured from a low-resolution cube, see Table 4 of Nordgren et al. (1997). Those authors found $M_{\text{HI}} = 3.6 \times 10^9 \text{ M}_{\odot}$, which is 60% of the Garland et al. (2004) single-dish value.

Table 5. Dynamical Masses from Cuts Along Major Axes

Galaxy	$V_{\text{opt}}^{\text{a}}$ (km s $^{-1}$)	$V_{\text{sys}}^{\text{b}}$ (km s $^{-1}$)	R_{25}^{c} (kpc)	$V_{\text{rot}}(R_{25})^{\text{d}}$ (km s $^{-1}$)	R_{HI}^{e} (arcsec)	R_{HI} (kpc)	$V_{\text{rot}}(R_{\text{HI}})^{\text{f}}$ (km s $^{-1}$)	$i_{\text{opt}}^{\text{g}}$ (deg)	$M_{\text{dyn}}(R_{25})$ ($10^{10} M_{\odot}$)	$M_{\text{dyn}}(R_{\text{HI}})$ ($10^{10} M_{\odot}$)
SDSS0119+1452 ^h	4118.6 \pm 13.6	4118.6 \pm 13.6	7.3 \pm 1.1	27.1 \pm 13.6	21.2 \pm 0.4	6.0 \pm 0.1	27.1 \pm 13.6	49.7	0.2 \pm 0.14	0.18 \pm 0.12
SDSS0125+0110	5877.1 \pm 13.7	5877.1 \pm 13.7	7.9 \pm 1.4	68.6 \pm 13.7	51.3 \pm 0.6	20.9 \pm 0.25	68.6 \pm 13.7	41.5	2.0 \pm 0.9	5.2 \pm 2.1
SDSS0728+3532	3944.1 \pm 13.5	3964.4 \pm 13.5	5.3 \pm 1.1	54.2 \pm 13.5	51.6 \pm 0.6	14.2 \pm 0.2	74.5 \pm 13.5	45.3	0.71 \pm 0.29	1.8 \pm 1.3
SDSS0934+0014	4905.8 \pm 13.6	4926.3 \pm 13.6	6.5 \pm 1.2	40.9 \pm 13.6 ⁱ	18.0 \pm 2.0	6.1 \pm 0.7	47.7 \pm 13.6	68.4	0.31 \pm 0.21	0.38 \pm 0.22
SDSS0936+0106	4883.5 \pm 13.1	4909.7 \pm 13.1	7.4 \pm 1.2	91.7 \pm 13.1	44.1 \pm 0.6	15.0 \pm 0.2	104.8 \pm 13.1	50.6	2.4 \pm 0.8	6.4 \pm 1.6
SDSS1319+5203	4657.4 \pm 13.6	4623.4 \pm 13.6	5.4 \pm 1.8	47.6 \pm 13.6	49.2 \pm 1.2	15.8 \pm 0.4	20.4 \pm 13.6	53.9	0.44 \pm 0.29	0.23 \pm 0.31
SDSS1402+0955	4213.0 \pm 13.6	4233.4 \pm 13.6	8.6 \pm 1.1	115.3 \pm 13.6	35.7 \pm 0.6	10.5 \pm 0.2	115.3 \pm 13.6	54.4	4.0 \pm 1.1	4.9 \pm 1.1
SDSS1507+5511	3347.9 \pm 13.5	3320.9 \pm 13.5	7.8 \pm 0.8	67.4 \pm 13.5	52.5 \pm 1.2	12.1 \pm 0.3	80.9 \pm 13.5	42.5	1.8 \pm 0.7	4.0 \pm 1.4
Mrk 325 ^h	3373.9 \pm 10.3	3368.8 \pm 10.3	7.2 \pm 0.8	25.8 \pm 10.3	23.0 \pm 1.0	5.5 \pm 0.2	25.8 \pm 10.3	68.2	0.13 \pm 0.10	0.10 \pm 0.07

^aVelocities are measured at the position of the optical galaxy along the major axis.

^bSystemic velocities are measured at the halfway point of the major axis along the H I diameter.

^c $R_{25}(\text{B})$ taken from Hyperleda.

^dUncorrected rotation velocity at $R_{25}(\text{B})$.

^e R_{HI} is the distance between the optical center of the galaxy and the contour with a column density of $1 \text{ M}_{\odot} \text{pc}^{-2}$.

^fUncorrected rotation velocity at R_{HI} .

^gInclinations taken from Hyperleda.

^hSDSS0119+1452 and Mrk 325 are less extended in H I than in the optical, so $V_{\text{rot}}(R_{25})$ is taken to be the velocity at R_{HI} .

ⁱThe H I of SDSS0934+0014 is less extended than the optical galaxy on one side. We took the velocity at the side where the H I is more extended than the optical galaxy.

Table 6. Dynamical Masses from Rotation Curve Fits

Galaxy	V_{sys} (km s ⁻¹)	PA (deg)	i_{fit} (deg)	$R_{\text{max}}^{\text{a}}$ (kpc)	$V_{\text{rot}}(R_{\text{max}})^{\text{b}}$ (km s ⁻¹)	$M_{\text{dyn}}(R_{\text{max}})$ (10 ¹⁰ M _⊙)
SDSS0119+1452	4133.81 ± 0.02	73.02 ± 0.03	48.37 ± 0.13	21.6 ± 0.7	40.7 ± 0.23	0.83 ± 0.03
SDSS0125+0110	5871.92 ± 0.07	53.84 ± 0.06	15.60 ± 0.89	14.5 ± 0.2	278.2 ± 14.3	26.1 ± 2.7
SDSS0728+3532	3940.67 ± 0.66	138.74 ± 0.35	43.41 ± 2.46	26.2 ± 6.3	117.4 ± 8.4	8.4 ± 2.4
SDSS0934+0014 ^c	4888.20 ± 85.00	57.08 ± 12.75	88.58 ± 6.72
SDSS0936+0106	4908.48 ± 0.27	293.25 ± 0.13	34.82 ± 1.19	35.6 ± 3.7	228.5 ± 9.4	43.3 ± 5.7
SDSS1319+5203 ^c	4626.34 ± 1.02	70.35 ± 12.47	-96.03 ± 30.43
SDSS1402+0955 ^d	4221.27 ± 0.01	6.98 ± 0.02	49.16 ± 0.21	20.9 ± 0.3	238.4 ± 1.6	27.6 ± 0.5
SDSS1507+5511 ^d	3338.38 ± 0.03	304.37 ± 0.08	39.74 ± 1.74	30.4 ± 2.8	140.5 ± 7.5	14.0 ± 2.0
Mrk 325	3377.12 ± 0.16	167.36 ± 0.29	54.98 ± 0.93	8.4 ± 1.5	30.24 ± 1.18	0.19 ± 0.03

^aRadius where the fitted velocity was at maximum.

^bMaximum fitted velocity, corrected for inclination.

^cFit did not converge for R_{max} or V_{max} .

^dFit only converged when center position was held fixed.

Table 7. Comparison of H I properties to those derived from single dish data

Galaxy	$V_{\text{rot}}^{\text{G04a}}$ (km s ⁻¹)	$V_{\text{rot}}(\text{R}_{\text{HI}})^{\text{b}}$ (km s ⁻¹)	$R_{\text{HI}}^{\text{G04c}}$ (kpc)	R_{HI} (kpc)	$M_{\text{dyn}}^{\text{G04}}(\text{R}_{\text{HI}})^{\text{d}}$ (10 ¹⁰ M _⊙)	$M_{\text{dyn}}(\text{R}_{\text{HI}})^{\text{e}}$ (10 ¹⁰ M _⊙)	M_* (10 ¹⁰ M _⊙)	$f_{\text{gas}}^{\text{G04f}}$	$f_{\text{gas}}^{\text{g}}$
SDSS0119+1452	115	36	11.2	6.0	3.3	0.18	0.13	0.06	0.5
SDSS0125+0110	...	104	...	20.9	...	5.2	0.43	...	0.1
SDSS0728+3532 ^h	160	105	10.8	14.2	6.7	1.8	0.19	0.09	0.4
SDSS0934+0014	189	51	13.6	6.1	10.8	0.38	0.66	0.05	0.7
SDSS0936+0106	146	136	14.2	15.0	6.3	6.4	0.51	0.06	0.04
SDSS1319+5203 ^h	120	25	10.6	15.8	4.0	0.23	0.085	0.2	5.0
SDSS1402+0955	186	142	17.4	10.5	15.0	4.9	0.63	0.04	0.09
SDSS1507+5511	72	120	15.8	12.1	2.0	4.0	0.20	0.1	0.05
Mrk 325	121	28	19.2	9.1	6.3	0.1	0.31	0.1	0.4 ⁱ

^a $V_{\text{rot}}^{\text{G04}}$ is calculated using half of W_{20} , which is corrected for inclination and random motions and taken from Table 3 of Garland et al. (2004).

^b $V_{\text{rot}}(\text{R}_{\text{HI}})$ is measured using a cut along the major axis and is taken from Table 5 and corrected for inclination.

^c $R_{\text{HI}}^{\text{G04}}$ is estimated to be $2 \times R_{25}$ and is taken from Garland et al. (2004).

^d $M_{\text{dyn}}^{\text{G04}}(\text{R}_{\text{HI}})$ is calculated using the M_{HI} and $M_{\text{HI}}M_{\text{dyn}}^{-1}$ values in Table 3 and Table 4 of Garland et al. (2004).

^e $M_{\text{dyn}}(\text{R}_{\text{HI}})$ is calculated using $V_{\text{rot}}(\text{R}_{\text{HI}})$ and R_{HI} and is taken from Table 5.

$$f_{\text{gas}}^{\text{G04}} = M_{\text{HI}}/M_{\text{dyn}}^{\text{G04}}$$

$$f_{\text{gas}}^{\text{g}} = M_{\text{HI}}/M_{\text{dyn}}$$

^hSDSS0728+3532 and SDSS1319+5203 lie within H I envelopes that include other galaxies. Their H I masses include the entire envelope, while their rotation velocities and dynamical masses calculated from a cut along their major axes include only the LCBGs.

ⁱSince $M_{\text{HI}}/M_{\text{dyn}} > 1$, likely due to an underestimation of M_{dyn} due to uncertainty in the inclination, we report $f_{\text{gas}} = M_{\text{HI}}/(M_{\text{HI}} + M_*)$.

Table 8. Velocity dispersions

Galaxy	$\sigma_{R_{\text{eff}}}^{\text{a}}$ (km s ⁻¹)	$V_{\text{rot}}^{R_{\text{eff}}}{}^{\text{b}}$ (km s ⁻¹)	$\frac{V_{\text{rot}}^{R_{\text{eff}}}}{\sigma_{R_{\text{eff}}}}^{\text{c}}$	$\sigma_{R_{25}}^{\text{c}}$ (km s ⁻¹)	$V_{\text{rot}}^{R_{25}}{}^{\text{d}}$ (km s ⁻¹)	$\frac{V_{\text{rot}}^{R_{25}}}{\sigma_{R_{25}}}^{\text{e}}$
	$\sigma_{R_{\text{HI}}}^{\text{e}}$ (km s ⁻¹)	$\sigma_{>R_{25}}^{\text{f}}$ (km s ⁻¹)	$V_{\text{rot}}^{R_{\text{HI}}}{}^{\text{g}}$ (km s ⁻¹)	$\frac{V_{\text{rot}}^{R_{\text{HI}}}}{\sigma_{R_{\text{HI}}}}^{\text{h}}$	$\frac{V_{\text{rot}}^{R_{\text{HI}}}}{\sigma_{>R_{25}}}^{\text{h}}$	$t_{\text{ins}}^{\text{h}}$ (Gyr)
SDSS0119+1452 ⁱ	20.7 ± 0.8	8.9 ± 17.8	0.43 ± 0.86	12.1 ± 6.7	35.5 ± 17.8	2.9 ± 2.2
	12.6 ± 6.3	29.5 ± 3.4	35.5 ± 17.8	2.8 ± 2.0	1.2 ± 0.6	1.3
SDSS0125+0110	23.0 ± 3.2	62.1 ± 20.7	2.7 ± 1.0	20.1 ± 4.3	103.5 ± 20.7	5.2 ± 1.5
	11.2 ± 6.6	8.7 ± 5.2	103.5 ± 20.7	9.2 ± 5.8	11.9 ± 7.5	17
SDSS0728+3532	40.3 ± 1.6	28.6 ± 19.0	0.71 ± 0.47	33.0 ± 5.2	76.3 ± 19.0	2.3 ± 0.7
	20.6 ± 11.1	10.0 ± 7.3	104.8 ± 19.0	5.1 ± 2.9	10.5 ± 7.9	3.4
SDSS0934+0014	41.8 ± 0.9	7.3 ± 14.6	0.18 ± 0.35	34.6 ± 8.7	44.0 ± 14.6	1.3 ± 0.5
	35.3 ± 8.2	12.3 ± 13.6	51.3 ± 14.6	1.5 ± 0.5	4.2 ± 4.8	0.2
SDSS0936+0106	45.8 ± 5.4	67.8 ± 17.0	1.5 ± 0.4	30.5 ± 10.0	118.7 ± 17.0	3.9 ± 1.4
	21.0 ± 12.7	9.4 ± 7.4	135.6 ± 17.0	6.5 ± 4.0	14.4 ± 11.5	4.5
SDSS1319+5203	37.4 ± 4.3	8.4 ± 16.8	0.23 ± 0.45	39.5 ± 7.0	58.9 ± 16.8	1.5 ± 0.5
	24.7 ± 14.3	16.8 ± 12.6	25.2 ± 16.8	1.0 ± 0.9	1.5 ± 1.5	0.6
SDSS1402+0955	47.4 ± 4.7	41.7 ± 16.7	0.88 ± 0.36	31.5 ± 14.5	141.8 ± 16.7	4.5 ± 2.1
	27.1 ± 16.1	7.3 ± 9.7	141.8 ± 16.7	5.2 ± 3.2	19.4 ± 25.9	2.0
SDSS1507+5511	22.6 ± 1.9	10.0 ± 20.0	0.44 ± 0.89	18.5 ± 7.5	99.8 ± 20.0	5.4 ± 2.3
	15.2 ± 8.3	8.7 ± 8.1	119.7 ± 20.0	7.9 ± 4.5	13.8 ± 13.0	6.1
Mrk 325 ⁱ	15.7 ± 4.2	16.7 ± 11.1	1.1 ± 0.8	13.2 ± 6.0	27.8 ± 11.1	2.1 ± 1.3
	13.4 ± 5.9	13.1 ± 6.3	27.8 ± 11.1	2.1 ± 1.2	2.1 ± 1.3	1.4

^a $\sigma_{R_{\text{eff}}}$ is the average value of the Moment 2 map within R_{eff} .

^b $V_{\text{rot}}^{R_{\text{eff}}}$ is the rotation velocity measured at R_{eff} corrected for inclination.

^c $\sigma_{R_{25}}$ is the average value of the Moment 2 map within R_{25} .

^d $V_{\text{rot}}^{R_{25}}$ is the rotation velocity measured at R_{25} corrected for inclination.

^e $\sigma_{R_{\text{HI}}}$ is the average value of the Moment 2 map within R_{HI} .

^f $\sigma_{>R_{25}}$ is the average value of the Moment 2 map outside of R_{25} .

^g $V_{\text{rot}}^{R_{\text{HI}}}$ is the rotation velocity measured at R_{HI} corrected for inclination

^h t_{ins} is the inspiral time for clumps to reach the center of a rotating disk.

ⁱ R_{25} is larger than the H I radius of SDSS0119+1452 and Mrk 325.

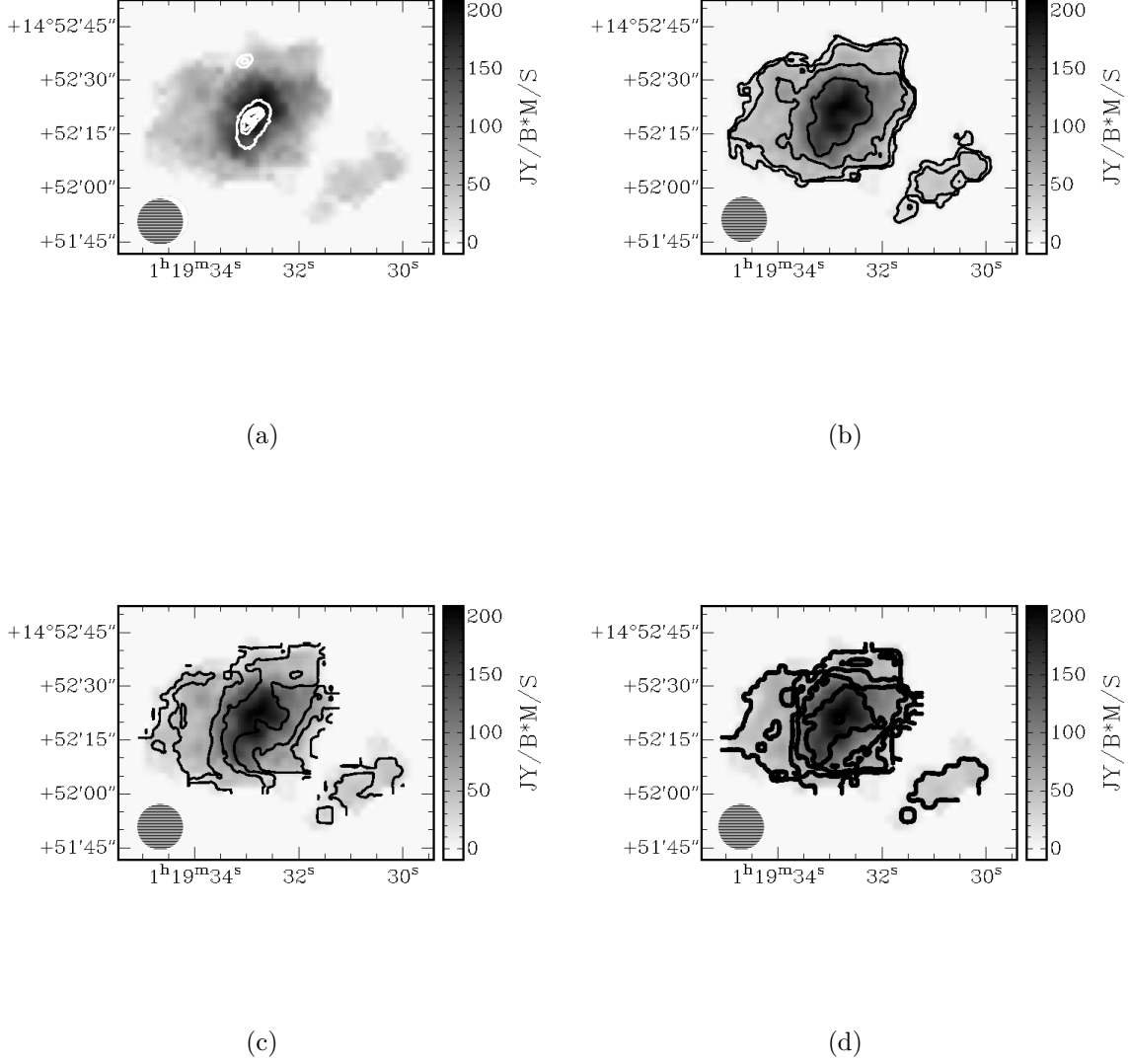


Fig. 1.—: Moment maps for SDSS0119+1452 (NGC 469) made with a $13'' \times 13''$ beam. The beam size is shown in the lower left corner. (a) Contours represent optical SDSS g intensity on an arbitrary scale overlaid on a Moment 0 grayscale. Contours were chosen to represent the positions and extent of the optical emission. (b) Contours are $2^n \times 10^{20} \text{ cm}^{-2}$ for $n = 0, 1, 2, 3$ taken from the Moment 0 map overlaid on a Moment 0 grayscale. (c) Contours are 10 km s^{-1} taken from the Moment 1 map overlaid on a Moment 0 grayscale. (d) Contours are 5 km s^{-1} from 5 km s^{-1} to 20 km s^{-1} taken from the Moment 2 map overlaid on a Moment 0 grayscale.

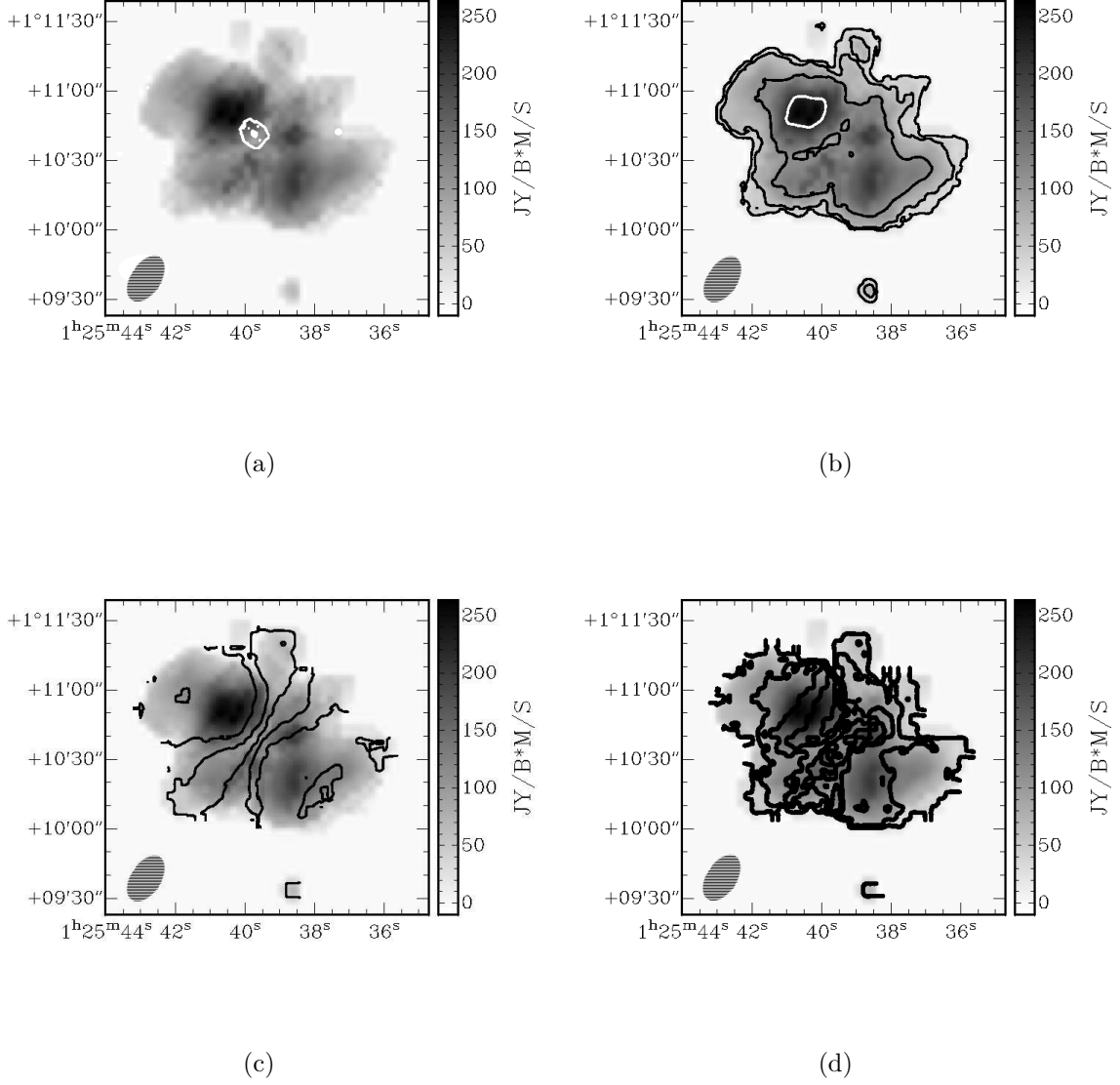


Fig. 2.—: Moment maps for SDSS0125+0110 (ARK 044) made with a $22'' \times 13''$ beam. The beam size is shown in the lower left corner. (a) Contours represent optical SDSS g intensity on an arbitrary scale overlaid on a Moment 0 grayscale. Contours were chosen to represent the positions and extent of the optical emission. (b) Contours are $2^n \times 10^{20} \text{ cm}^{-2}$ for $n = 0, 1, 2, 3$ taken from the Moment 0 map overlaid on a Moment 0 grayscale. (c) Contours are 25 km s^{-1} taken from the Moment 1 map overlaid on a Moment 0 grayscale. (d) Contours are 5 km s^{-1} from 5 km s^{-1} to 25 km s^{-1} taken from the Moment 2 map overlaid on a Moment 0 grayscale.

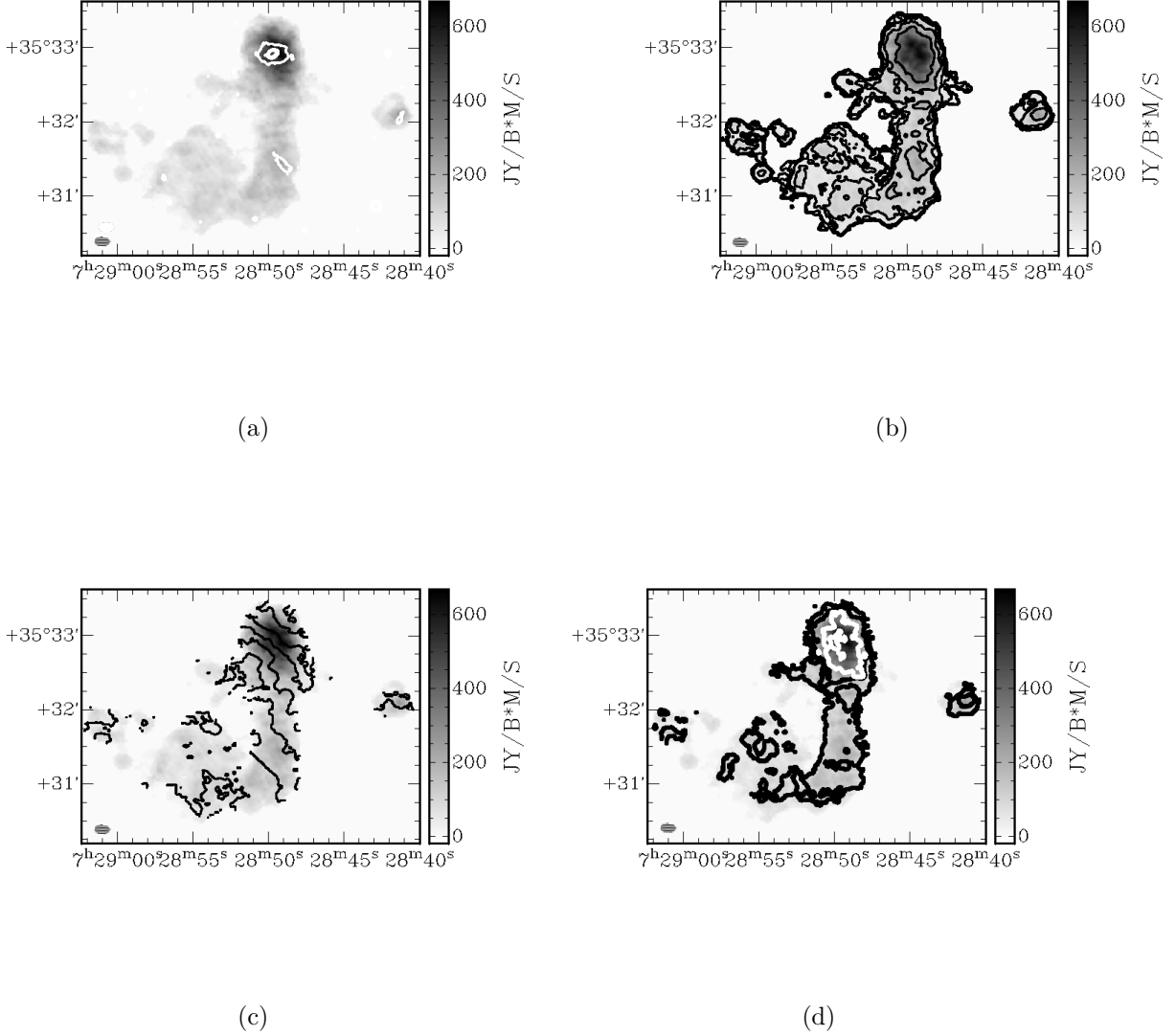


Fig. 3.—: Moment maps for SDSS0728+3532 (ARK 134) and its companions made with a $13'' \times 8''$ beam. The beam size is shown in the lower left corner. (a) Contours represent optical SDSS g intensity on an arbitrary scale overlaid on a Moment 0 grayscale. Contours were chosen to represent the positions and extent of the optical emission. (b) Contours are $2^n \times 10^{20} \text{ cm}^{-2}$ for $n = 0, 1, 2, 3, 4, 5$ taken from the Moment 0 map overlaid on a Moment 0 grayscale. (c) Contours are 25 km s^{-1} taken from the Moment 1 map overlaid on a Moment 0 grayscale. (d) Contours are 10 km s^{-1} from 10 km s^{-1} to 40 km s^{-1} taken from the Moment 2 map overlaid on a Moment 0 grayscale.

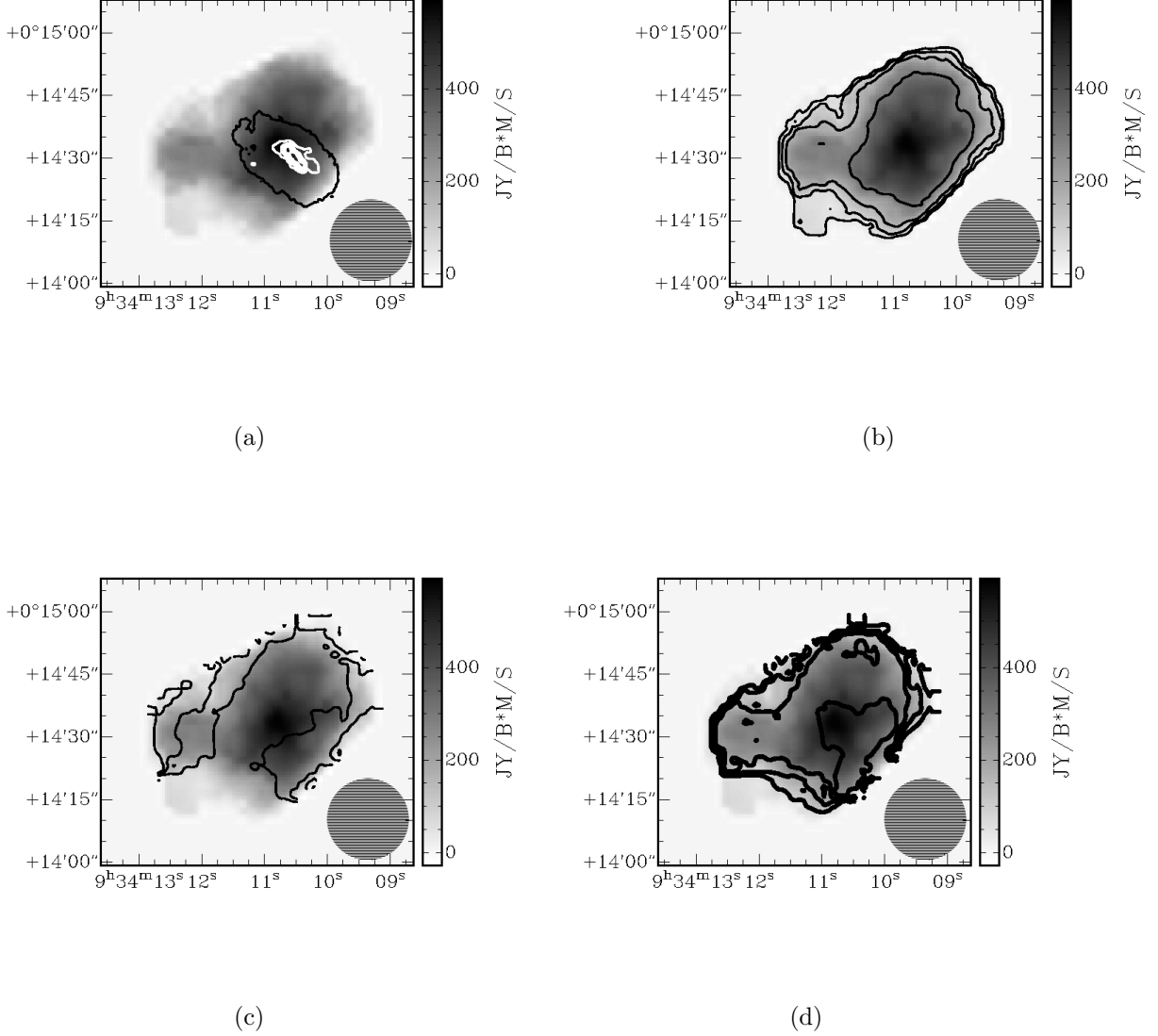


Fig. 4.—: Moment maps for SDSS0934+0014 (UGC 05097) made with a $20'' \times 20''$ beam. The beam size is shown in the lower right corner. (a) Contours represent optical SDSS g intensity on an arbitrary scale overlaid on a Moment 0 grayscale. Contours were chosen to represent the positions and extent of the optical emission. (b) Contours are $2^n \times 10^{20} \text{ cm}^{-2}$ for $n = 0, 1, 2, 3$ taken from the Moment 0 map overlaid on a Moment 0 grayscale. (c) Contours are 25 km s^{-1} taken from the Moment 1 map overlaid on a Moment 0 grayscale. (d) Contours are 10 km s^{-1} from 10 km s^{-1} to 50 km s^{-1} taken from the Moment 2 map overlaid on a Moment 0 grayscale.

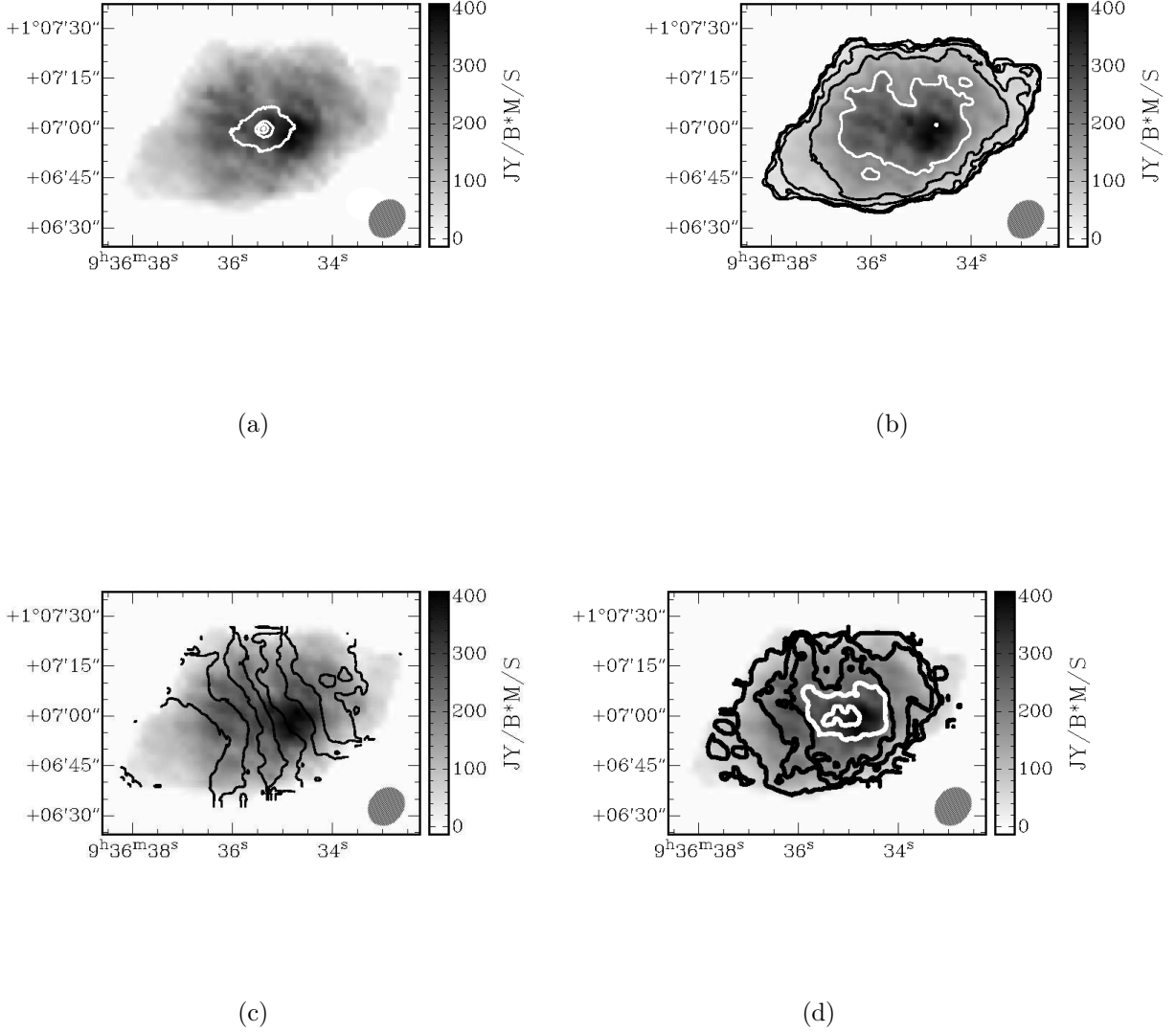


Fig. 5.—: Moment maps for SDSS0936+0106 (CGCG 007-009) made with a $21'' \times 11''$ beam. The beam size is shown in the lower right corner. (a) Contours represent optical SDSS g intensity on an arbitrary scale overlaid on a Moment 0 grayscale. Contours were chosen to represent the positions and extent of the optical emission. (b) Contours are $2^n \times 10^{20} \text{ cm}^{-2}$ for $n = 0, 1, 2, 3, 4, 5$ taken from the Moment 0 map overlaid on a Moment 0 grayscale. (c) Contours are 25 km s^{-1} taken from the Moment 1 map overlaid on a Moment 0 grayscale. (d) Contours are 10 km s^{-1} from 10 km s^{-1} to 50 km s^{-1} taken from the Moment 2 map overlaid on a Moment 0 grayscale.

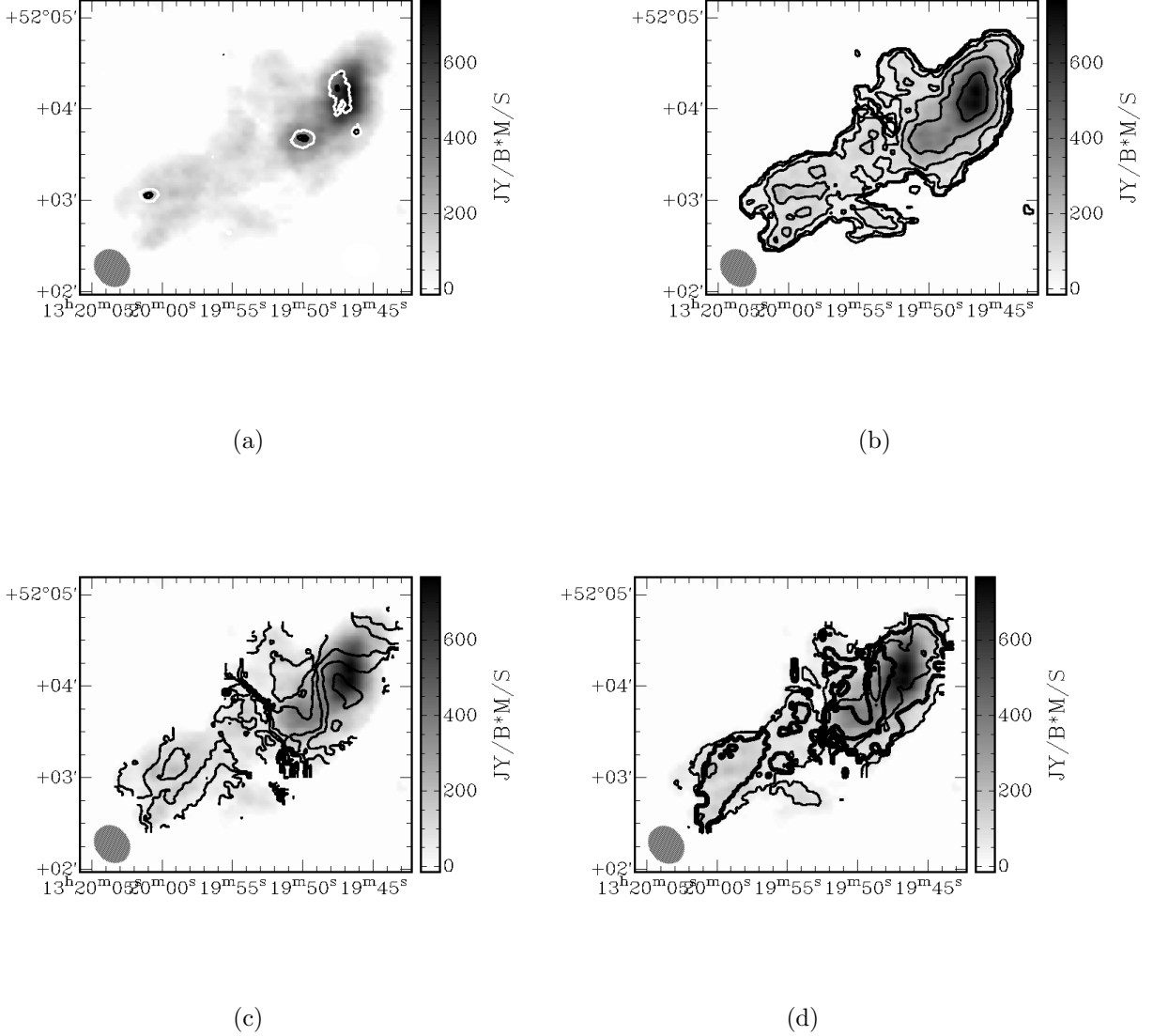


Fig. 6.—: Moment maps for SDSS1319+5203 (SBS 1317+523B) and its companions made with a $15'' \times 12''$ beam. The beam size is shown in the lower left corner. (a) Contours represent optical SDSS g intensity on an arbitrary scale overlaid on a Moment 0 grayscale. Contours were chosen to represent the positions and extent of the optical emission. (b) Contours are $2^n \times 10^{20} \text{ cm}^{-2}$ for $n = 0, 1, 2, 3, 4, 5$ taken from the Moment 0 map overlaid on a Moment 0 grayscale. (c) Contours are 25 km s^{-1} taken from the Moment 1 map overlaid on a Moment 0 grayscale. (d) Contours are 10 km s^{-1} from 10 km s^{-1} to 70 km s^{-1} taken from the Moment 2 map overlaid on a Moment 0 grayscale.

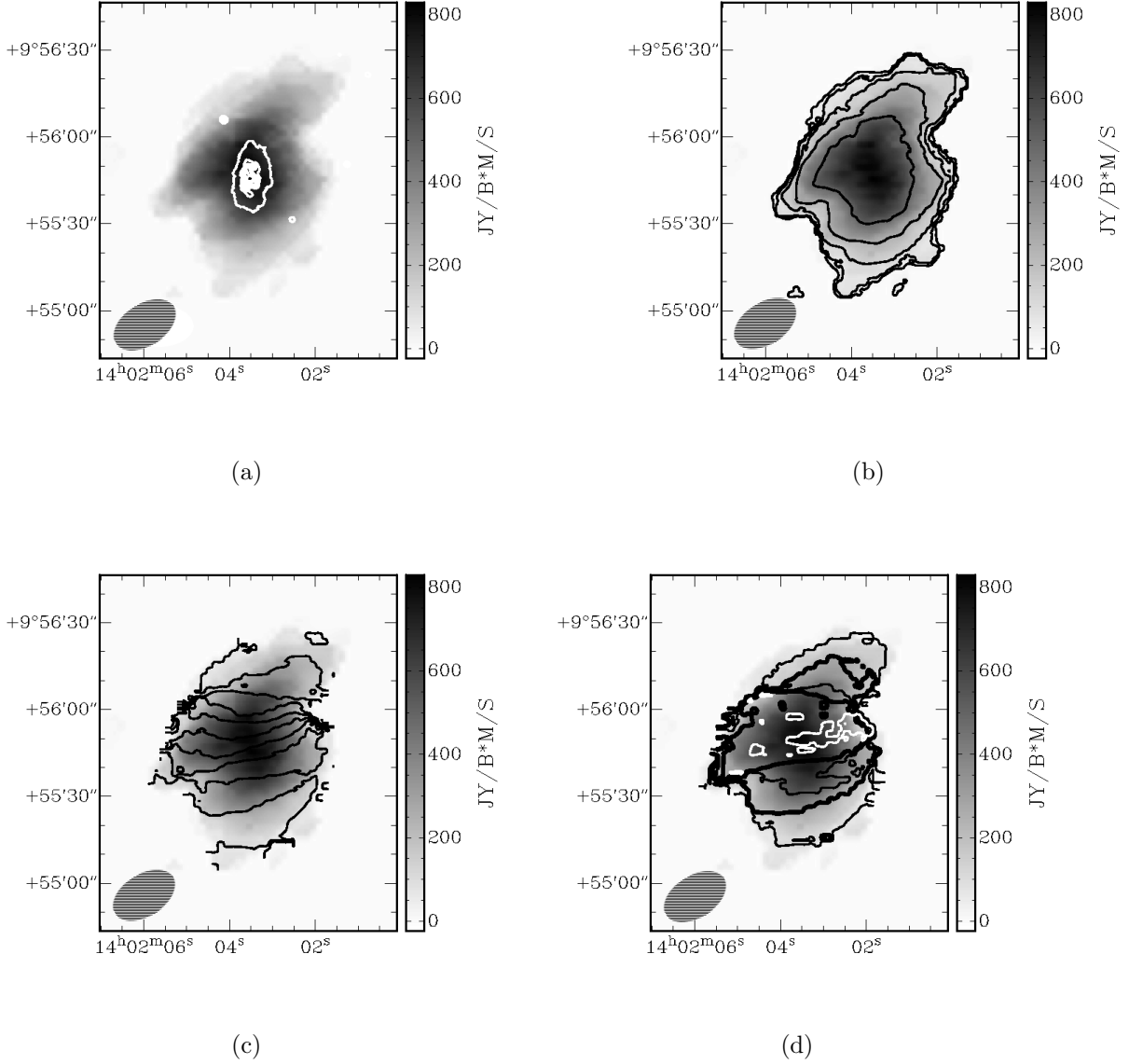


Fig. 7.—: Moment maps for SDSS1402+0955 (NGC 5414) made with a $23'' \times 14''$ beam. The beam size is shown in the lower left corner. (a) Contours represent optical SDSS g intensity on an arbitrary scale overlaid on a Moment 0 grayscale. Contours were chosen to represent the positions and extent of the optical emission. (b) Contours are $2^n \times 10^{20} \text{ cm}^{-2}$ for $n = 0, 1, 2, 3, 4$ taken from the Moment 0 map overlaid on a Moment 0 grayscale. (c) Contours are 25 km s^{-1} taken from the Moment 1 map overlaid on a Moment 0 grayscale. (d) Contours are 10 km s^{-1} from 10 km s^{-1} to 70 km s^{-1} taken from the Moment 2 map overlaid on a Moment 0 grayscale.

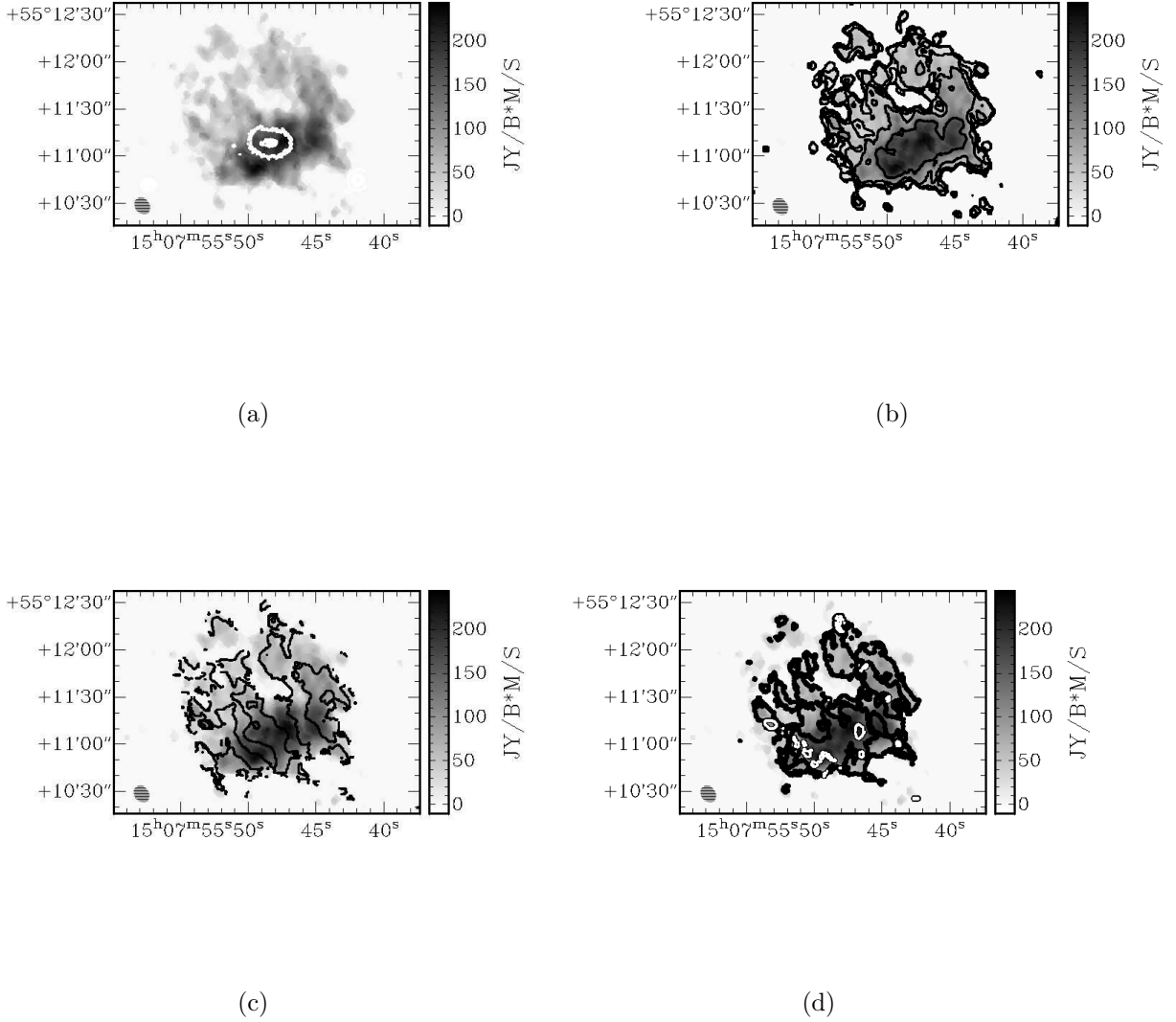


Fig. 8.—: Moment maps for SDSS1507+5511 (UGC 09737) made with a $11'' \times 9''$ beam. The beam size is shown in the lower left corner. (a) Contours represent optical SDSS g intensity on an arbitrary scale overlaid on a Moment 0 grayscale. Contours were chosen to represent the positions and extent of the optical emission. (b) Contours are $2^n \times 10^{20} \text{ cm}^{-2}$ for $n = 0, 1, 2, 3, 4$ taken from the Moment 0 map overlaid on a Moment 0 grayscale. (c) Contours are 25 km s^{-1} taken from the Moment 1 map overlaid on a Moment 0 grayscale. (d) Contours are 10 km s^{-1} from 10 km s^{-1} to 30 km s^{-1} taken from the Moment 2 map overlaid on a Moment 0 grayscale.

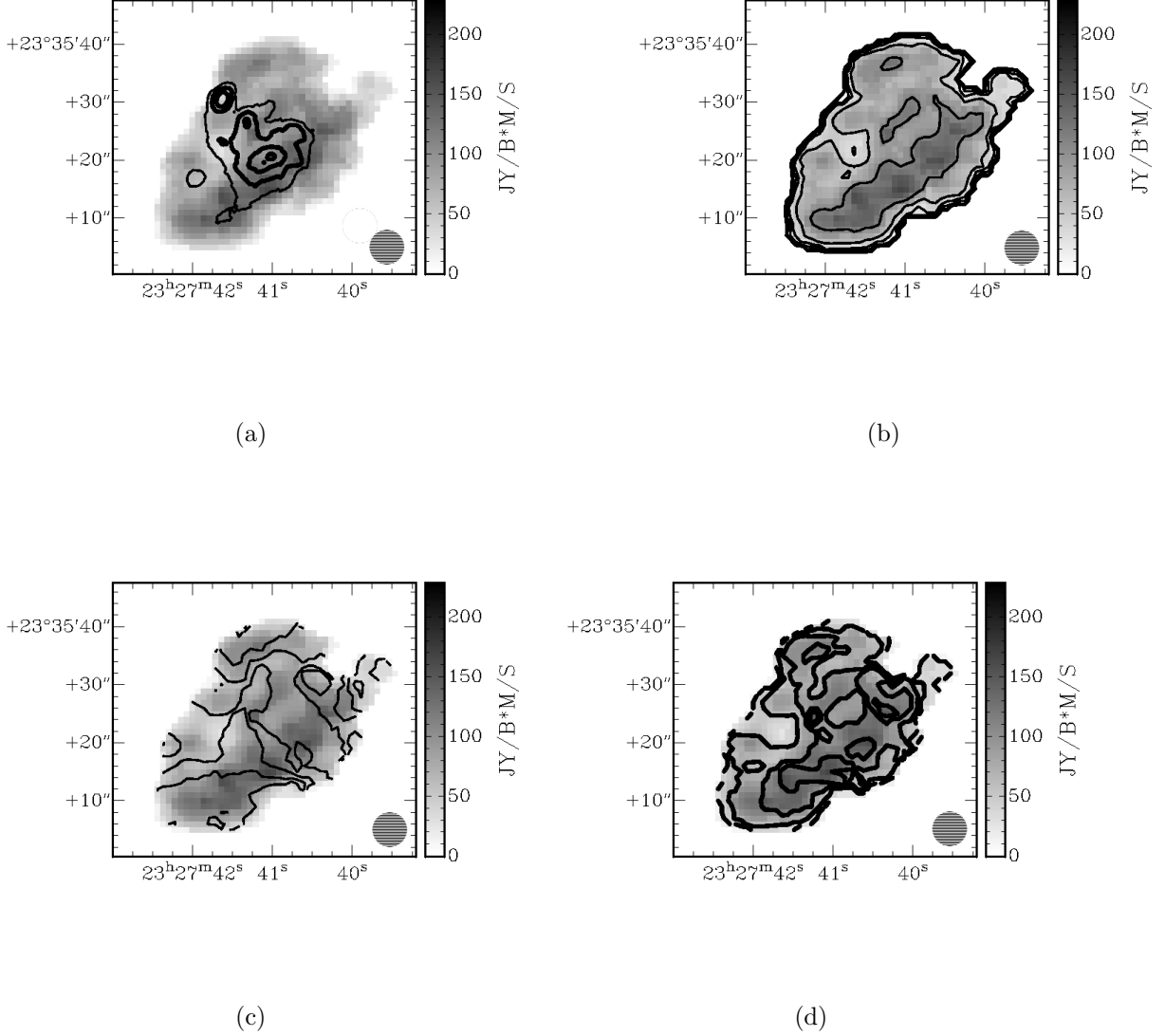


Fig. 9.—: Moment maps for Mrk 325 (NGC 7673) made with a $6'' \times 6''$ beam. The beam size is shown in the lower right corner. (a) Contours represent optical SDSS g intensity on an arbitrary scale overlaid on a Moment 0 grayscale. Contours were chosen to represent the positions and extent of the optical emission. (b) Contours are $2^n \times 10^{20} \text{ cm}^{-2}$ for $n = 0, 1, 2, 3, 4, 5$ taken from the Moment 0 map overlaid on a Moment 0 grayscale. (c) Contours are 10 km s^{-1} taken from the Moment 1 map overlaid on a Moment 0 grayscale. (d) Contours are 5 km s^{-1} from 5 km s^{-1} to 25 km s^{-1} taken from the Moment 2 map overlaid on a Moment 0 grayscale.

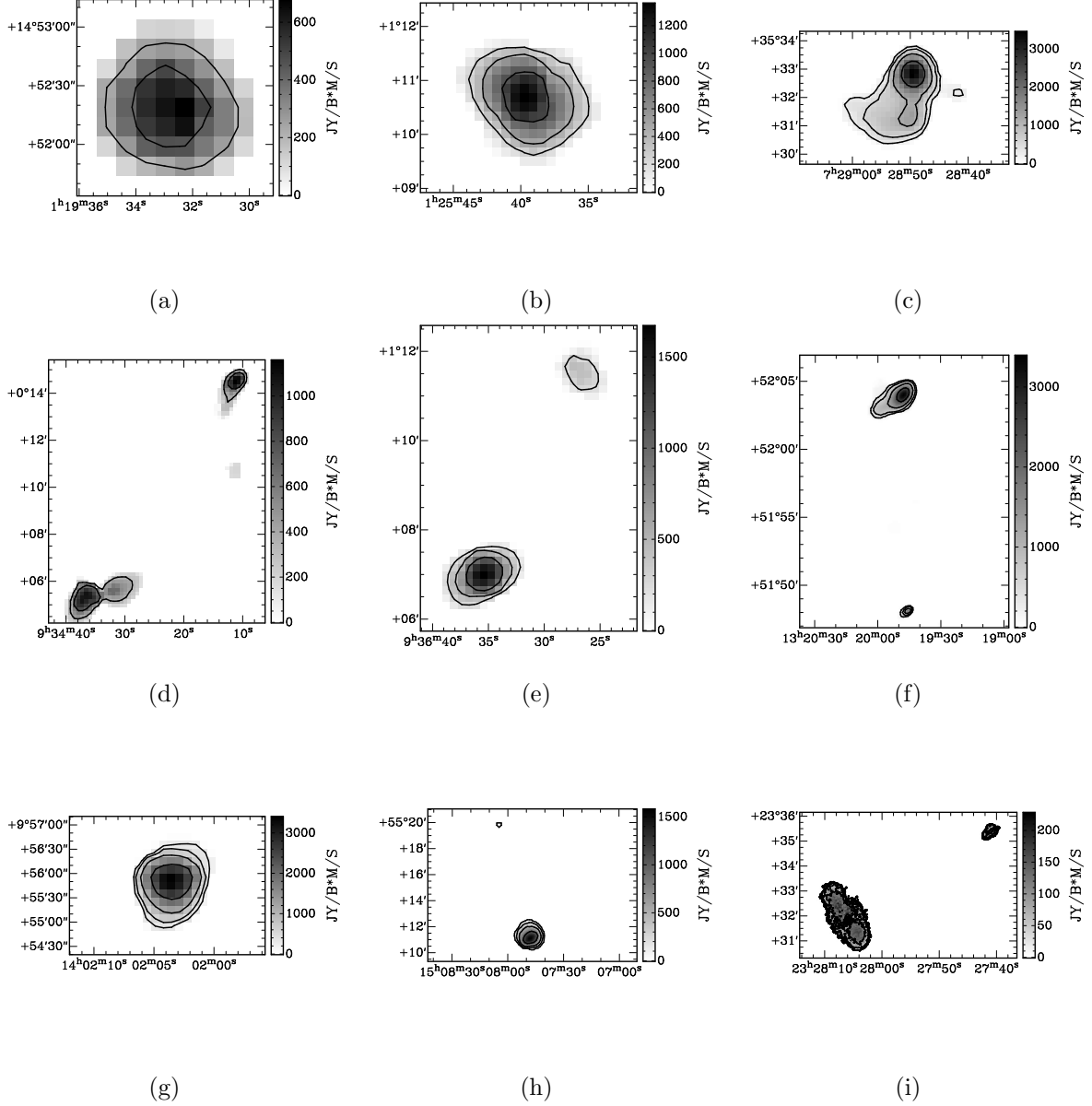


Fig. 10.—: Low-resolution ($\theta \sim 1'$) Moment 0 maps of (a) SDSS 0119+1452, (b) SDSS0125+0110, (c) SDSS0728+3532, (d) SDSS0934+0014, (e) SDSS0936+0106, (f) SDSS1319+5203, (g) SDSS1402+0955, (h) SDSS1507+5511, and (i) $\theta \sim 6''$ Moment 0 map of Mrk 325. Contours are $2^n \times 10^{20} \text{ cm}^{-2}$. The fields of view were chosen to include detected companions. For a $\theta \sim 1'$ moment map of Mrk 325, see Figure 17 of Nordgren et al. (1997).

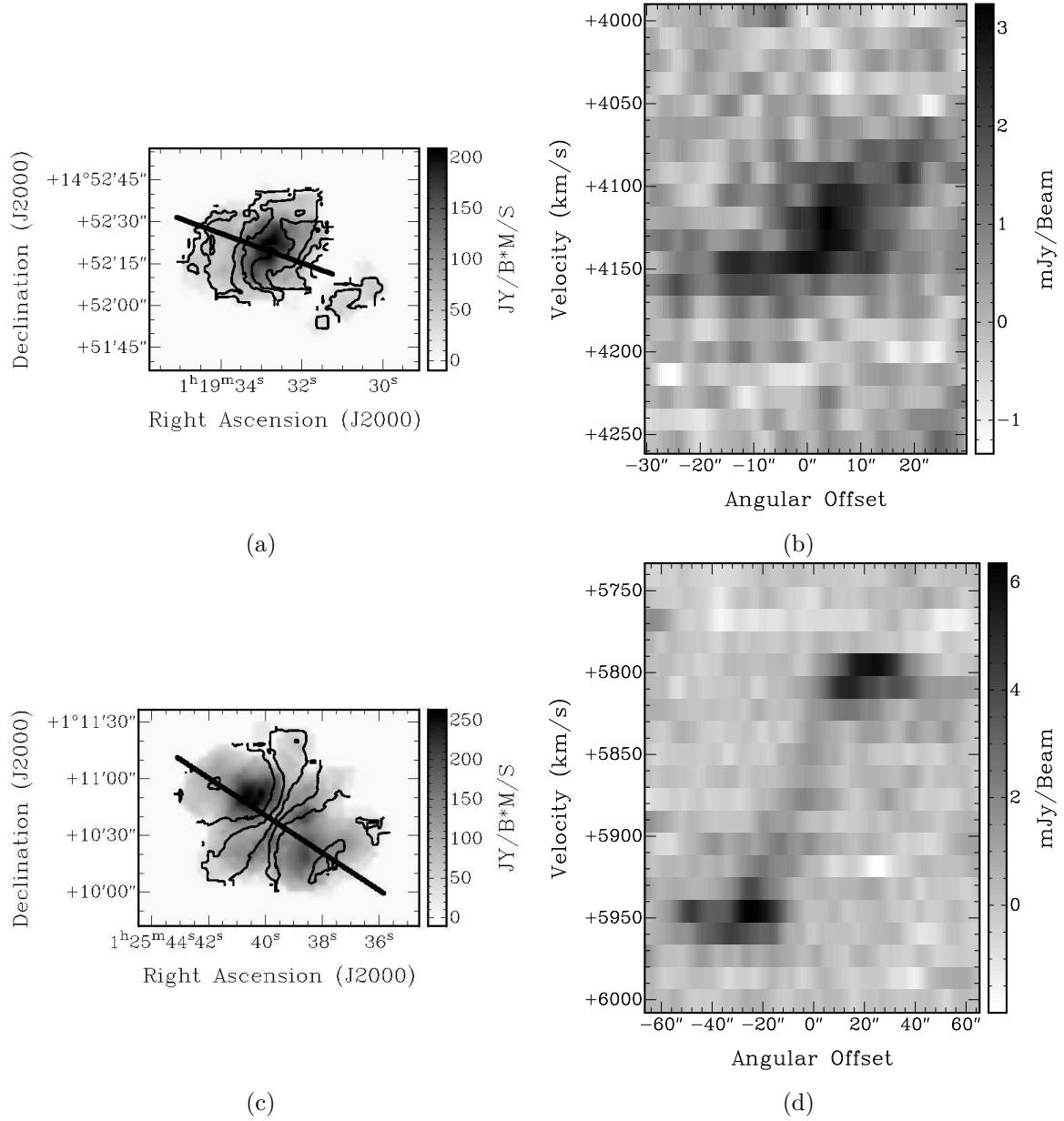


Fig. 11.—: (Left) Moment 0 map of each galaxy (grayscale) with Moment 1 contours (black) and major axis (thick black line) overlaid. (Right) Position-velocity plot of each galaxy along its major axis.

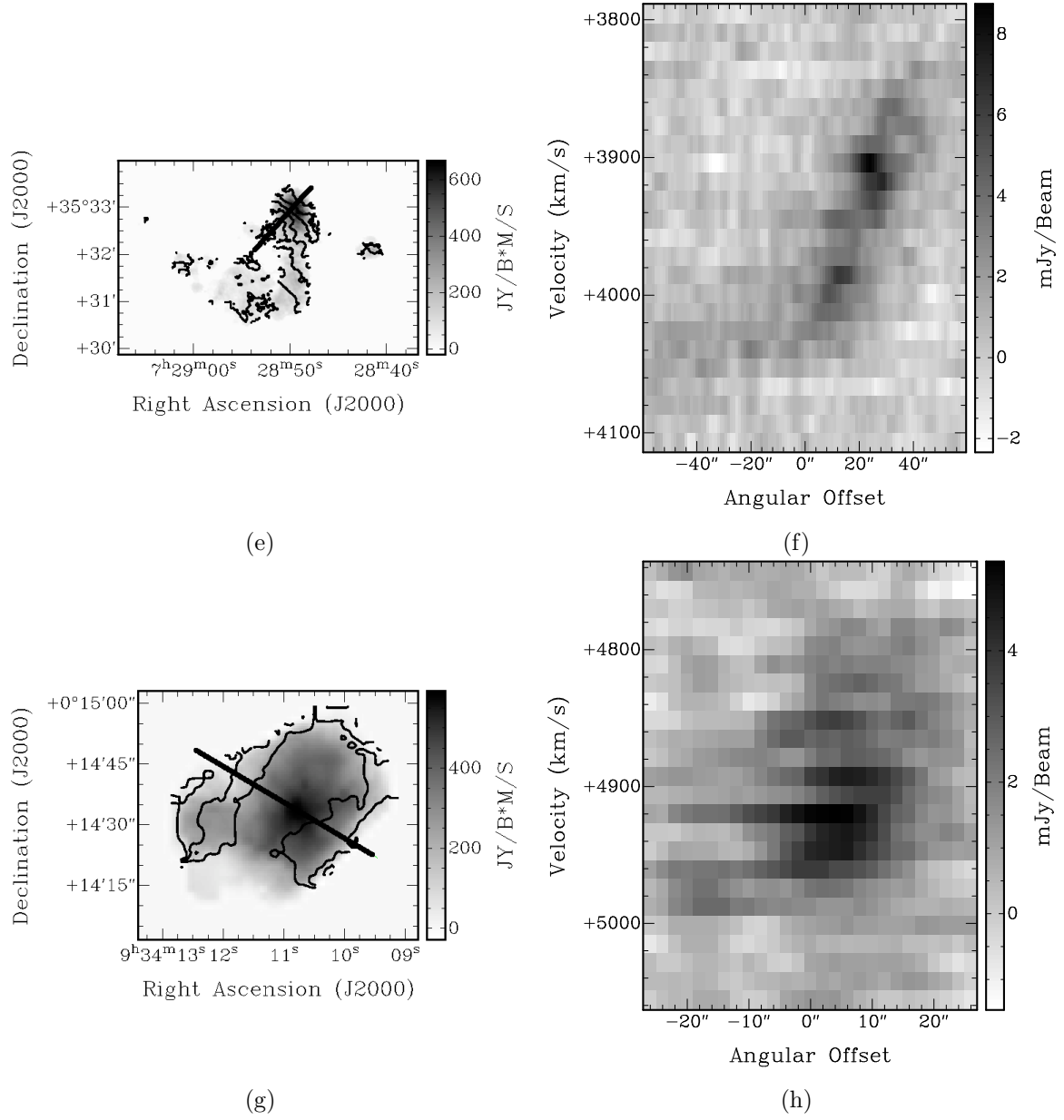


Fig. 11.—: Continued.

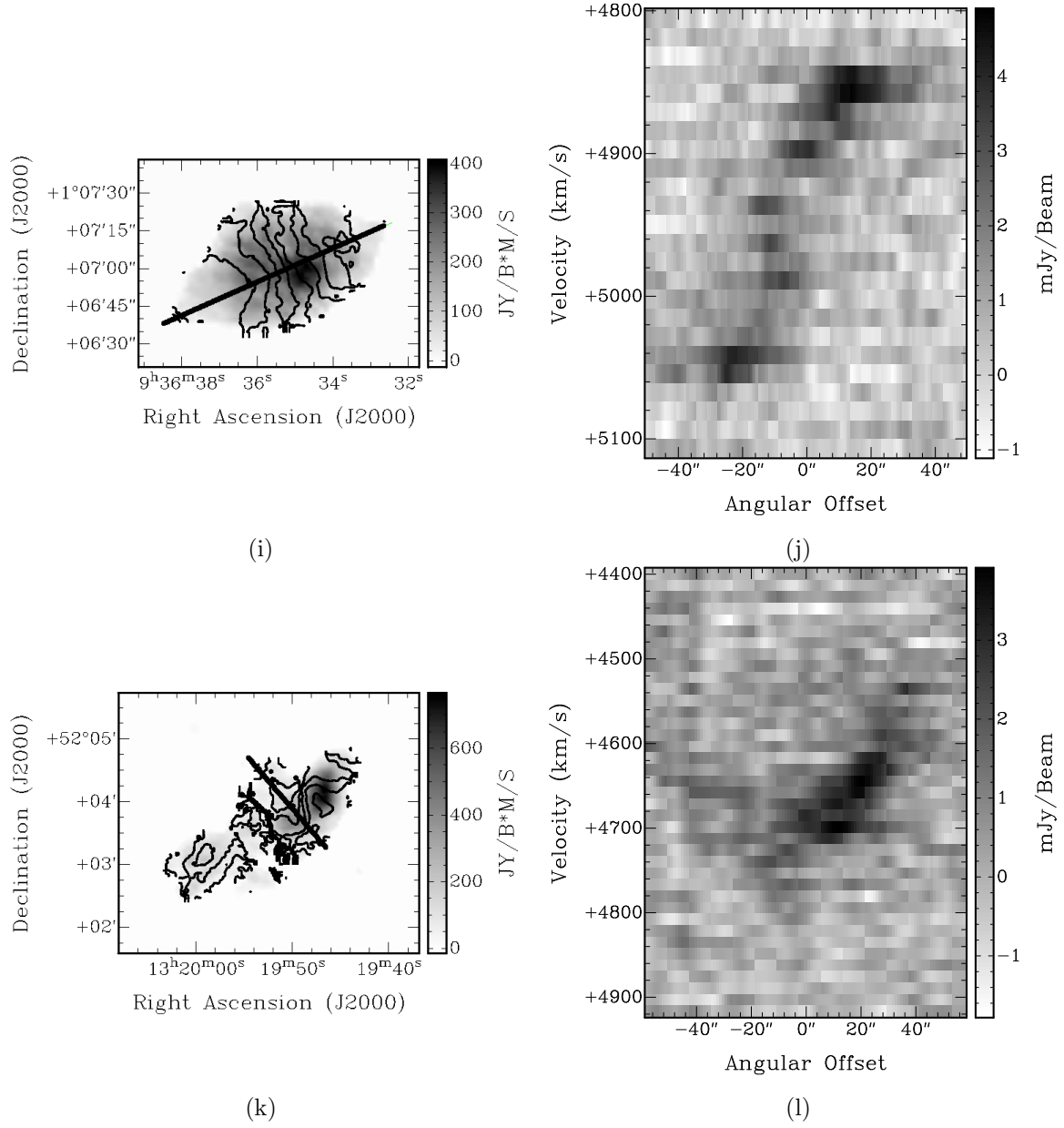


Fig. 11.—: Continued.

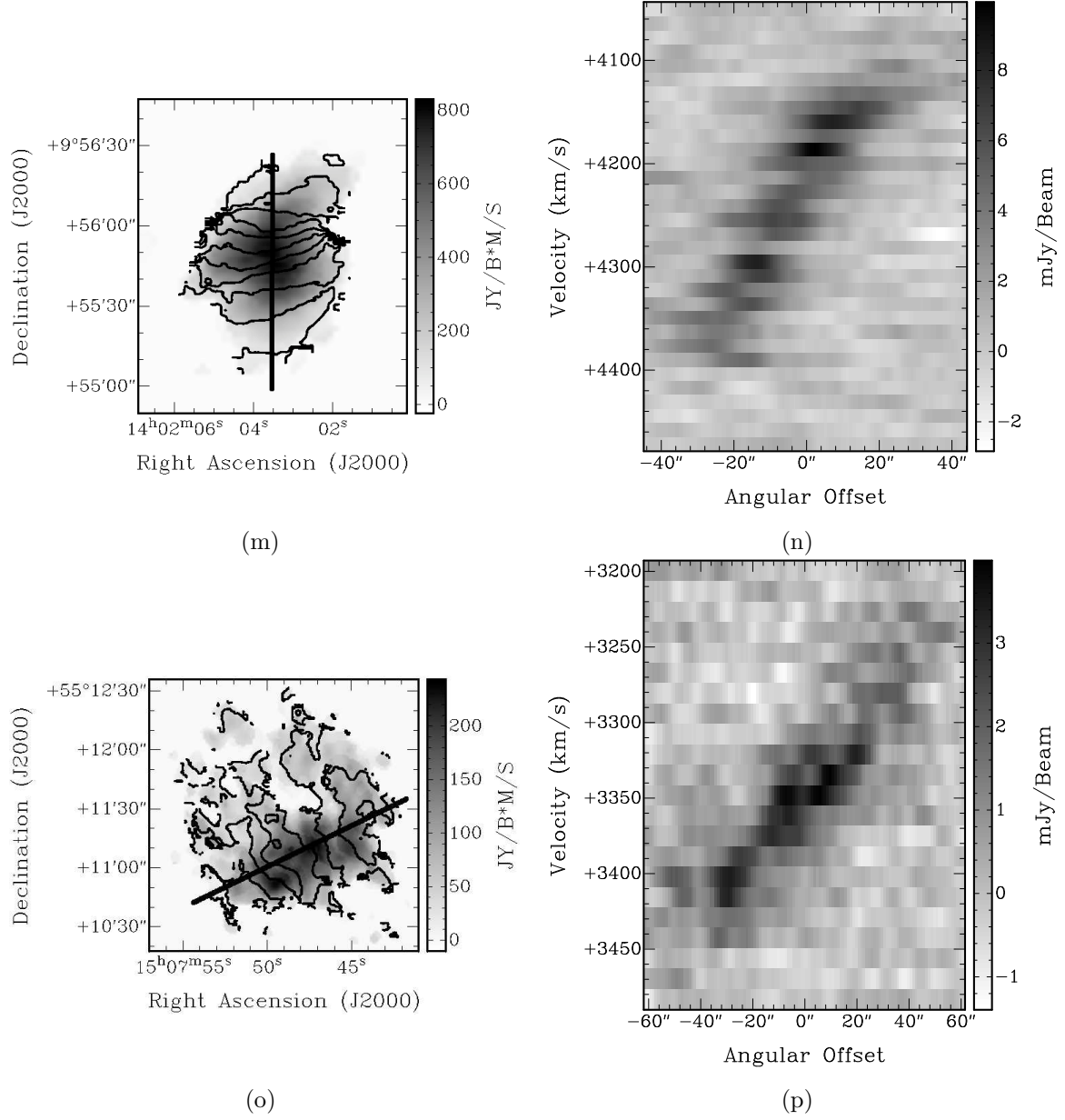


Fig. 11.—: Continued.

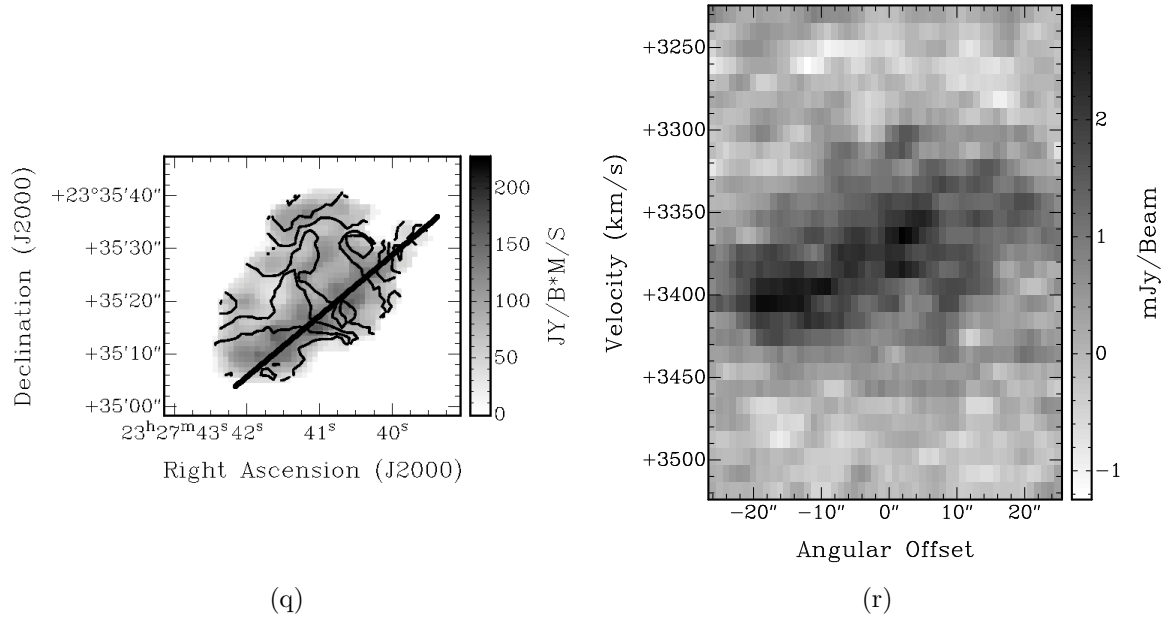


Fig. 11.—: Continued.

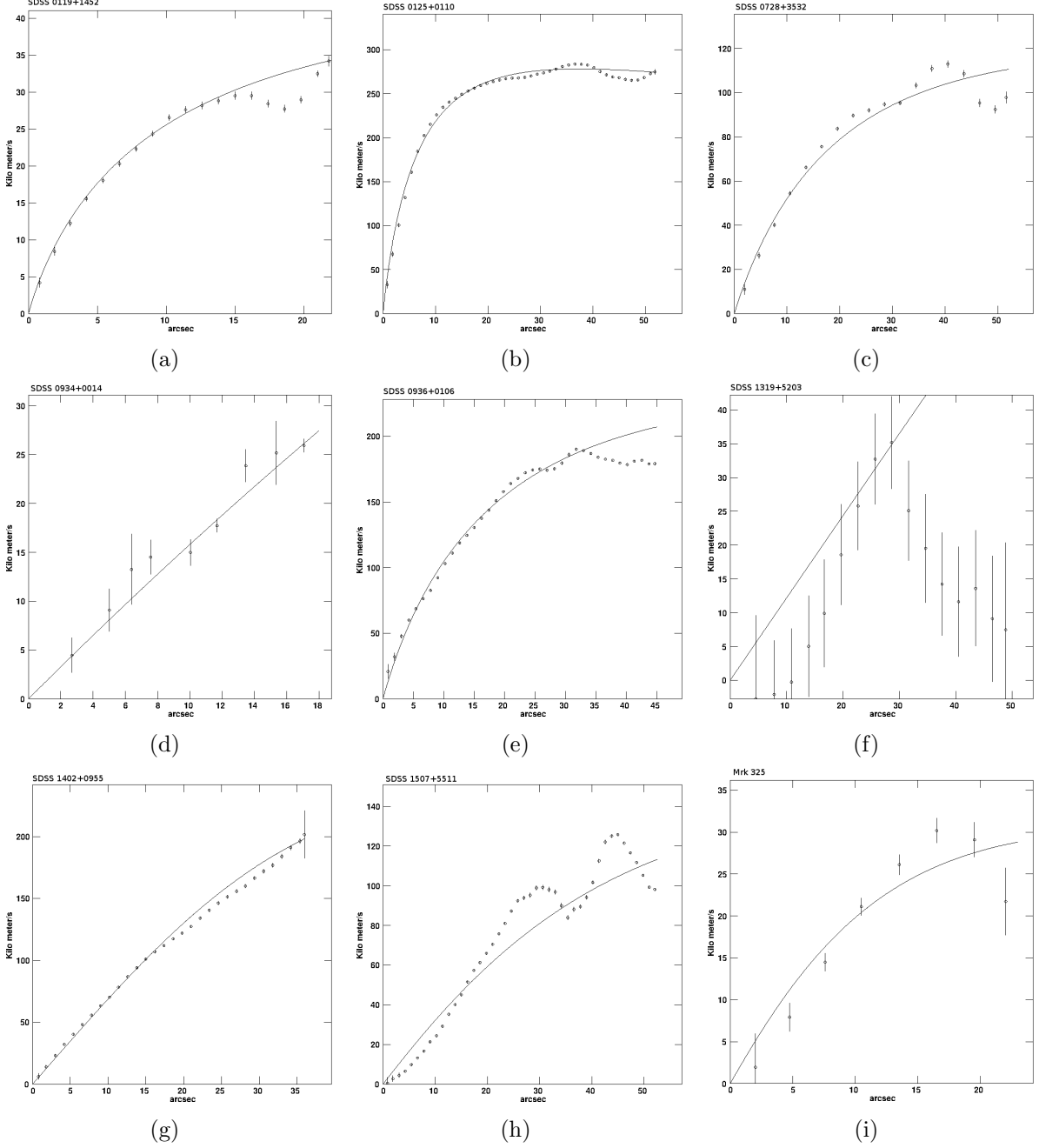


Fig. 12.—: Rotation curves fit using the AIPS task GAL. The curves are restricted to be fit within R_{HI} .

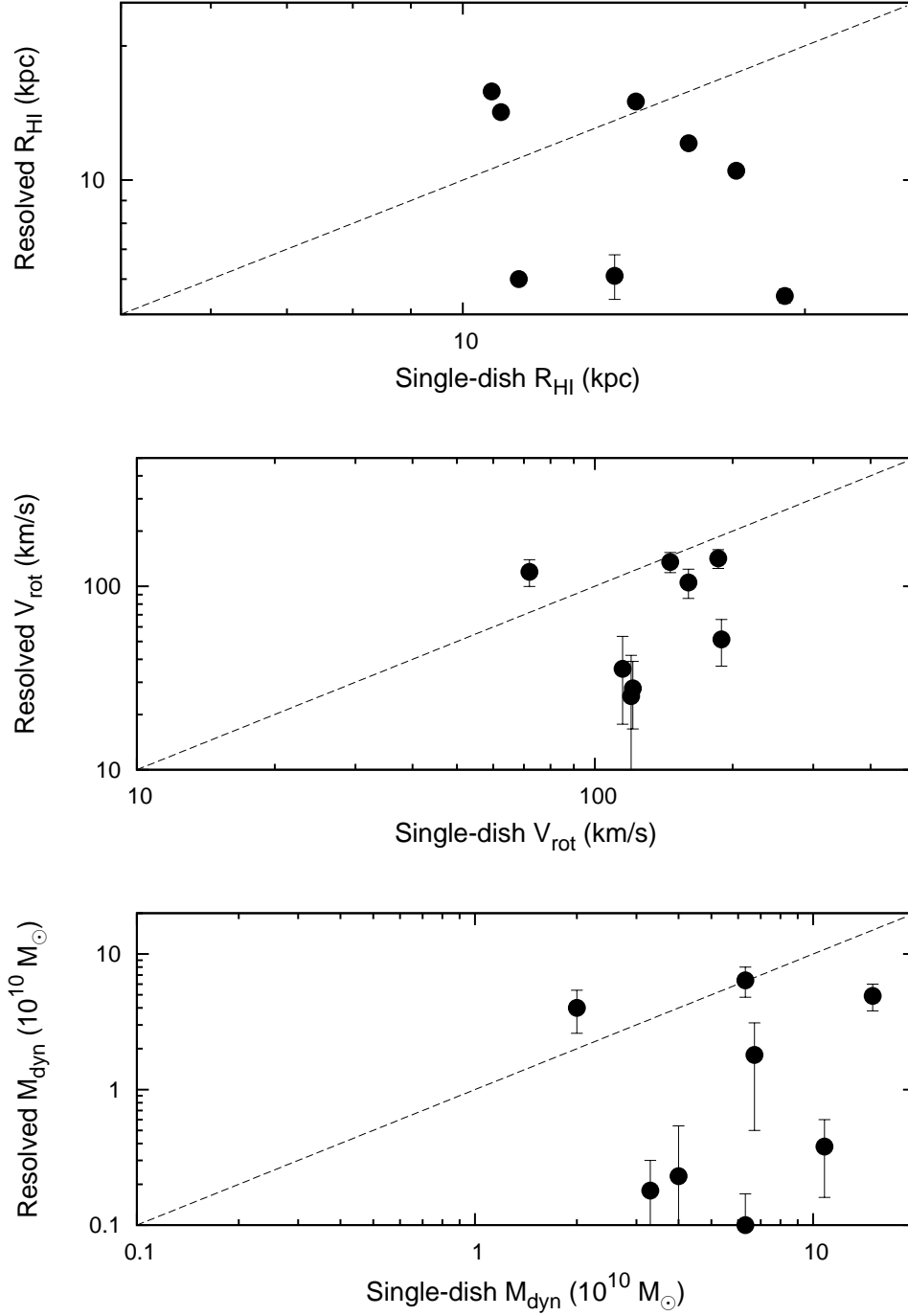


Fig. 13.—: R_{HI} (top), V_{rot} (middle), and M_{dyn} (bottom) using data from Garland et al. (2004) and our measurements for the LCBGs common to both samples. Garland et al. (2004) estimated R_{HI} to be $R_{\text{HI}} = 2 \times R_{25}$, and used half of the width of each galaxy’s single-dish H I spectrum corrected for inclination and random motions as V_{rot} . The dashed black lines show a 1:1 relationship between the two data sets. In some cases, error bars are smaller than point sizes.

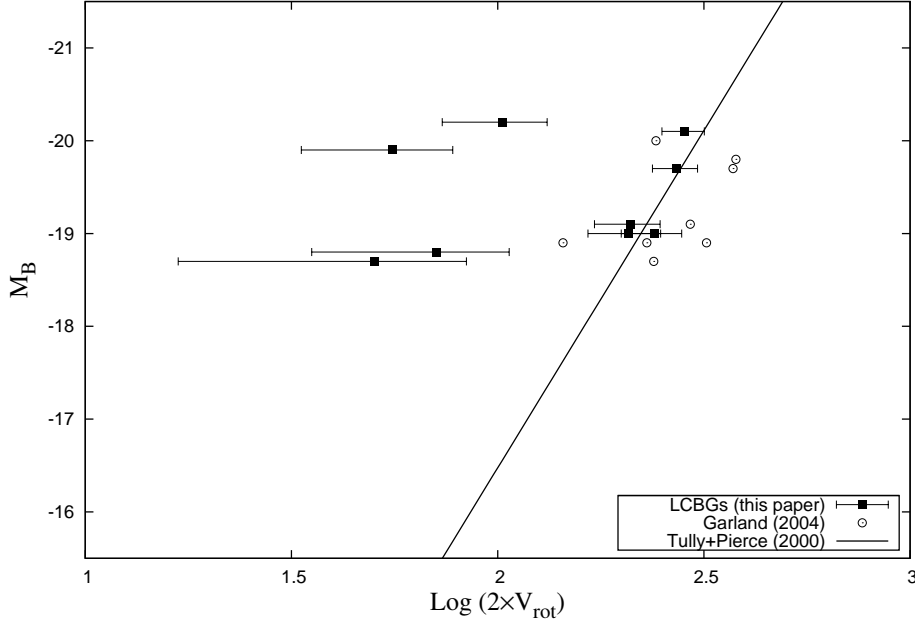


Fig. 14.—: A version of the Tully-Fisher relation, described in Tully & Pierce (2000). M_B for the LCBGs in our sample (filled squares) are calculated as described in Garland et al. (2004) using SDSS g and r magnitudes and distances taken from Table 1. Their V_{rot} values are taken from cuts across the galaxies’ major axes and corrected for inclination. The same LCBGs (with the exception of SDSS0125+0110) are plotted with M_B and linewidths corrected for random motions and inclinations taken from Table 1 and Table 3 of Garland et al. (2004) (open circles). The Tully-Fisher relation as described in Tully & Pierce (2000) is plotted with the black line. Notice that four of the LCBGs in our sample are much brighter in the B band than their V_{rot} values would suggest, while six of the LCBGs in the Garland et al. (2004) sample are faint in the B band with respect to their linewidths. We find that the LCBGs in our sample either follow the Tully-Fisher relation or have the ability to evolve onto it once their star formation is quenched and their M_B subsequently fade. We interpret the galaxies lying to the right of the Tully-Fisher relation from the Garland et al. (2004) sample as having overestimated rotation velocities due to the inclusion of non-rotation H I features or companion galaxies in the beam.

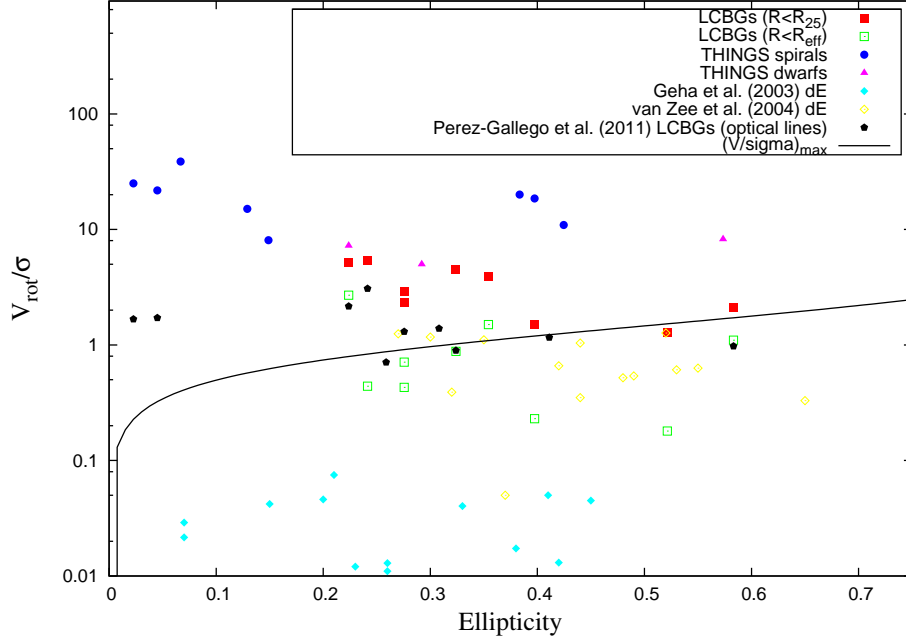


Fig. 15.—: $V_{\text{rot}}\sigma^{-1}$ plotted against ellipticity ($\epsilon = 1 - b/a$) for a variety of galaxy samples. The solid black curve is the maximum value of $V_{\text{rot}}\sigma^{-1}$ allowed for elliptical galaxies. Galaxies above this curve are too rotation-supported to be classified as elliptical galaxies. The points represent the LCBGs in our sample measured within R_{25} (filled squares) and R_{eff} (open squares), spiral galaxies from the THINGS sample (filled circles), dwarf galaxies from the THINGS sample (filled triangles), dwarf elliptical galaxies with a measured rotation component from Geha et al. (2003) (filled diamonds) and van Zee et al. (2004) (open diamonds), and for LCBGs in the Pérez-Gallego et al. (2011) sample (filled stars). ϵ values are taken from Hyperleda except for the Geha et al. (2003) sample, where ϵ is taken from Table 3 of that paper, and the van Zee et al. (2004) sample, where ϵ is taken from Table 1 of that paper. LCBG V_{rot} values are measured using a cut along the galaxies’ major axes. THINGS (Tamburro et al. 2009) σ values are the average H I σ values measured within R_{HI} . THINGS V_{rot} values are taken using half of W_{20} corrected for inclination from Walter et al. (2008). Geha et al. (2003) dwarf elliptical V_{rot} and σ values are measured from optical absorption lines within $0.5-1 R_{\text{eff}}$. van Zee et al. (2004) dwarf elliptical V_{rot} and σ values are measured from optical absorption lines within the last point where a rotation curve could be fit. Pérez-Gallego et al. (2011) V_{rot} values are measured from rotation curves fit to H α velocity maps, and σ values are measured from [OIII] λ 5007 maps.

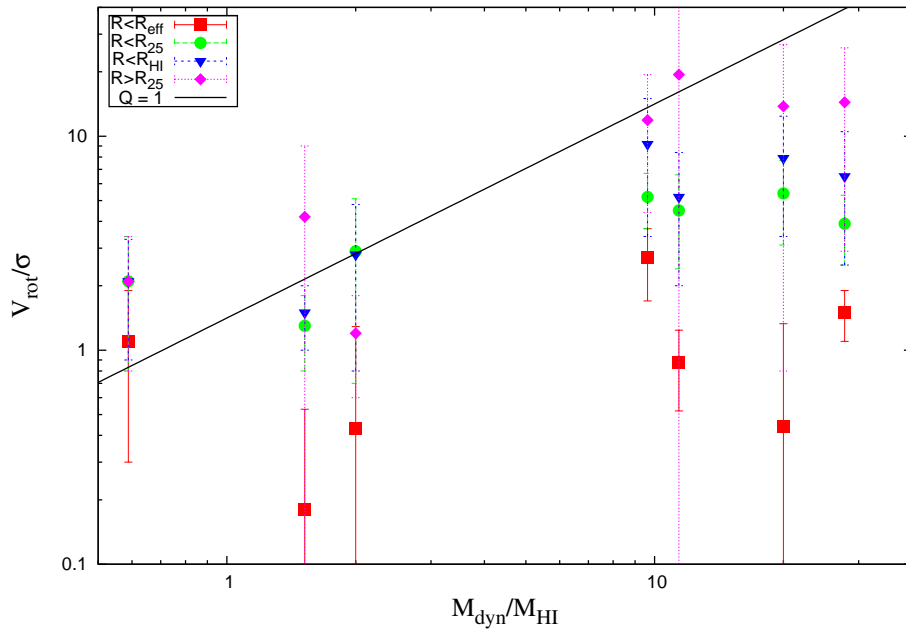


Fig. 16.—: $V_{\text{rot}}\sigma^{-1}$ within R_{eff} (red squares), R_{25} (green circles), R_{HI} (blue triangles) and outside of R_{25} (purple diamonds) for the LCBGs in our sample that do not share a common H I envelope with another galaxy. The solid line is the Toomre criterion for disk instability for a gas disk (Toomre 1964). Above the line, galaxies’ disks can develop local instabilities. Below the line, turbulence prevents gas clumps from forming. Over their entire disks, LCBGs are mostly stable.

REFERENCES

- Abazajian, K. N., Adelman-McCarthy, J. K., Agüeros, M. A., et al. 2009, *ApJS*, 182, 543
- Amram, P., Östlin, G. 2001, *The Messenger*, 103, 31
- Barton, E. J., & van Zee, L. 2001, *ApJ*, 550, L35
- Barton, E. J., van Zee, L., & Bershady, M. A. 2006, *ApJ*, 649, 129
- Bell, E. F., & de Jong, R. S. 2001, *ApJ*, 550, 212
- Bershady, M. A., Vils, M., Hoyos, C., Guzmán, R., & Koo, D. C. 2005, *Starbursts: From 30 Doradus to Lyman Break Galaxies*, 329, 177
- Brandt, J. C. 1960, *ApJ*, 131, 293
- Broeils, A. H., & van Woerden, H. 1994, *A&AS*, 107, 129
- Cardamone, C., Schawinski, K., Sarzi, M., et al. 2009, *MNRAS*, 399, 1191
- Crawford, S. M., Wirth, G. D., Bershady, M. A., & Hon, K. 2011, *ApJ*, 741, 98
- Crawford, S. M., Wirth, G. D., & Bershady, M. A. 2014, *ApJ*, 786, 30
- Dekel, A., Sari, R., & Ceverino, D. 2009, *ApJ*, 703, 785
- Elmegreen, B. G., Elmegreen, D. M., Fernandez, M. X., & Lemonias, J. J. 2009, *ApJ*, 692, 12
- Förster Schreiber, N. M., Genzel, R., Bouché, N., et al. 2009, *ApJ*, 706, 1364
- France, K., Nell, N., Green, J. C., & Leitherer, C. 2010, *ApJ*, 722, L80
- Garland, C. A., Pisano, D. J., Williams, J. P., Guzmán, R., & Castander, F. J. 2004, *ApJ*, 615, 689
- Garland, C. A., Williams, J. P., Pisano, D. J., et al. 2005, *ApJ*, 624, 714
- Garland, C. A., Pisano, D. J., Williams, J. P., et al. 2007, *ApJ*, 671, 310
- Garland, C. A. et al., *ApJ* submitted
- Garland, C. A. et al. in prep
- Geha, M., Guhathakurta, P., & van der Marel, R. P. 2003, *AJ*, 126, 1794
- Genzel, R., Förster Schreiber, N. M., Lang, P., et al. 2014, *ApJ*, 785, 75
- Guzmán, R., Gallego, J., Koo, D. C., et al. 1997, *ApJ*, 489, 559

- Guzmán, R. 1999, *The Evolution of Galaxies on Cosmological Timescales*, 187, 271
- Guzmán, R. 2001, *Astrophysics and Space Science Supplement*, 277, 507
- Guzmán, R., Östlin, G., Kunth, D., et al. 2003, *ApJ*, 586, L45
- Hammer, F., Gruel, N., Thuan, T. X., Flores, H., & Infante, L. 2001, *ApJ*, 550, 570
- Harmanec, P. 1988, *Bulletin of the Astronomical Institutes of Czechoslovakia*, 39, 329
- Heckman, T. M., Hoopes, C. G., Seibert, M., et al. 2005, *ApJ*, 619, L35
- Hoyos, C., Guzmán, R., Bershad, M. A., Koo, D. C., & Díaz, A. I. 2004, *AJ*, 128, 1541
- Hoyos, C., Guzmán, R., Díaz, A. I., Koo, D. C., & Bershad, M. A. 2007, *AJ*, 134, 2455
- Inoue, S., & Saitoh, T. R. 2012, *MNRAS*, 422, 1902
- Kassin, S. A., Weiner, B. J., Faber, S. M., et al. 2012, *ApJ*, 758, 106
- Koo, D. C., Bershad, M. A., Wirth, G. D., Stanford, S. A., & Majewski, S. R. 1994, *ApJ*, 427, L9
- Kormendy, J., & Kennicutt, R. C., Jr. 2004, *ARA&A*, 42, 603
- Lintott, C., Schawinski, K., Bamford, S., et al. 2011, *MNRAS*, 410, 166
- Maeder, A., & Meynet, G. 1989, *A&A*, 210, 155
- Noeske, K. G., Koo, D. C., Phillips, A. C., et al. 2006, *ApJ*, 640, L143
- Noguchi, M. 1998, *Nature*, 392, 253
- Noguchi, M. 1999, *ApJ*, 514, 77
- Noguchi, M. 2000, *MNRAS*, 312, 194
- Noguchi, M. 2001, *ApJ*, 555, 289
- Nordgren, T. E., Chengalur, J. N., Salpeter, E. E., & Terzian, Y. 1997, *AJ*, 114, 77
- Östlin, G., Amram, P., Boulesteix, J., et al. 2001, *Astrophysics and Space Science Supplement*, 277, 433
- Overzier, R. A., Heckman, T. M., Tremonti, C., et al. 2009, *ApJ*, 706, 203
- Pérez-Gallego, J., Guzmán, R., Castillo-Morales, A., et al. 2010, *MNRAS*, 402, 1397
- Pérez-Gallego, J., Guzmán, R., Castillo-Morales, A., et al. 2011, *MNRAS*, 418, 2350
- Phillips, A. C., Guzmán, R., Gallego, J., et al. 1997, *ApJ*, 489, 543

- Pisano, D. J., Kobulnicky, H. A., Guzmán, R., Gallego, J., & Bershad, M. A. 2001, *AJ*, 122, 1194
- Romano, D., Chiappini, C., Matteucci, F., Tosi, M. 2005, *A&A*, 430, 491
- Sparke, L. S., & Gallagher, J. S., III 2007, *Galaxies in the Universe: An Introduction*. Second Edition. By Linda S. Sparke and John S. Gallagher, III. ISBN-13 978-0-521-85593-8 (HB); ISBN-13 978-0-521-67186-6 (PB). Published by Cambridge University Press, Cambridge, UK, 2007 .,
- Tamburro, D., Rix, H.-W., Leroy, A. K., et al. 2009, *AJ*, 137, 4424
- Tollerud, E. J., Barton, E. J., van Zee, L., & Cooke, J. 2010, *ApJ*, 708, 1076
- Tonini, C., Jones, D. H., Mould, J., et al. 2014, *MNRAS*, 438, 3332
- Toomre, A. 1964, *ApJ*, 139, 1217
- Tully, R. B., & Fisher, J. R. 1977, *ApJ*, 217, 661
- Tully, R. B., & Fouque, P. 1985, *ApJS*, 58, 67
- Tully, R. B., & Pierce, M. J. 2000, *ApJ*, 533, 744
- van Zee, L., Skillman, E. D., & Haynes, M. P. 2004, *AJ*, 128, 121
- Walter, F., Brinks, E., de Blok, W. J. G., et al. 2008, *AJ*, 136, 2563
- Werk, J. K., Jangren, A., & Salzer, J. J. 2004, *ApJ*, 617, 1004